AGU PUBLICATIONS

JGR

Journal of Geophysical Research: Oceans

RESEARCH ARTICLE

10.1002/2017JC013311

Wind Forced Variability in Eddy Formation, Eddy Shedding, and the Separation of the East Australian Current

Christopher Y. S. Bull[1,2], Andrew E. Kiss[2,3,4], Nicolas C. Jourdain[2,5], Matthew H. England[1,2], and Erik van Sebille[2,6,7]

[1]Climate Change Research Centre, University of New South Wales, Sydney, NSW, Australia, [2]ARC Centre of Excellence for Climate System Science, University of New South Wales, Sydney, NSW, Australia, [3]School of Physical, Environmental and Mathematical Sciences, University of New South Wales Canberra at the Australian Defence Force Academy, Canberra, ACT, Australia, [4]Research School of Earth Sciences, Australian National University, Canberra, ACT, Australia, [5]Université Grenoble Alpes, CNRS, IRD, IGE, Grenoble, France, [6]Grantham Institute and Department of Physics, Imperial College London, London, United Kingdom, [7]Institute for Marine and Atmospheric Research Utrecht, Utrecht University, Utrecht, The Netherlands

Abstract The East Australian Current (EAC), like many other subtropical western boundary currents, is believed to be penetrating further poleward in recent decades. Previous observational and model studies have used steady state dynamics to relate changes in the westerly winds to changes in the separation behavior of the EAC. As yet, little work has been undertaken on the impact of forcing variability on the EAC and Tasman Sea circulation. Here using an eddy-permitting regional ocean model, we present a suite of simulations forced by the same time-mean fields, but with different atmospheric and remote ocean variability. These eddy-permitting results demonstrate the nonlinear response of the EAC to variable, nonstationary inhomogeneous forcing. These simulations show an EAC with high intrinsic variability and stochastic eddy shedding. We show that wind stress variability on time scales shorter than 56 days leads to increases in eddy shedding rates and southward eddy propagation, producing an increased transport and southward reach of the mean EAC extension. We adopt an energetics framework that shows the EAC extension changes to be coincident with an increase in offshore, upstream eddy variance (via increased barotropic instability) and increase in subsurface mean kinetic energy along the length of the EAC. The response of EAC separation to regional variable wind stress has important implications for both past and future climate change studies.

Key Points:
- Regional wind stress variability of period $<\sim$2 months enhances East Australian Current (EAC) extension mean transport
- Regional wind stress variability drives increased baroclinic instability in the upstream EAC resulting in more frequent eddy shedding events
- EAC transport exhibits large intrinsic variability; remote forcing variability has limited impact on EAC variability and mean transport

Supporting Information:
- Supporting Information S1

Correspondence to:
C. Y. S. Bull,
christopher.ys.bull@gmail.com

Citation:
Bull, C. Y. S., Kiss, A. E., Jourdain, N. C., England, M. H., & van Sebille, E. (2017). Wind forced variability in eddy formation, eddy shedding, and the separation of the East Australian Current. *Journal of Geophysical Research: Oceans*, *122*, 9980–9998. https://doi.org/10.1002/2017JC013311

Received 28 JUL 2017
Accepted 15 NOV 2017
Accepted article online 17 NOV 2017
Published online 15 DEC 2017

1. Introduction

The East Australian Current (EAC) in the western South Pacific Ocean is Australia's strongest and most important boundary current, supporting Australia's temperate coastlines by transporting 1.35 $\pm$ 0.42 PW of heat poleward (Hu et al., 2015; Sloyan et al., 2016; Wu et al., 2012). At around 30°S–32°S the EAC partially bifurcates into the Tasman Front (Cetina-Heredia et al., 2014), and in the process of separating, the EAC sheds a large number of eddies in a region known as the EAC extension (Everett et al., 2012). These eddies propagate southwest toward Tasmania and a smaller portion continue around Tasmania into the Indian Ocean via a flow pathway known as the Tasman leakage (van Sebille et al., 2012). Via the Tasman leakage, the EAC participates in the Southern Hemisphere supergyre circulation, a key pathway of the global thermohaline circulation (Ridgway & Dunn, 2007; Speich et al., 2007).

Given the growing interest in the likelihood of changes in the midlatitude westerlies driving an enhancement of the EAC extension (Cai et al., 2005; Feng et al., 2016; Oliver & Holbrook, 2014; Ridgway, 2007; Roemmich et al., 2007, 2016; Sloyan & O'Kane, 2015), understanding the factors that influence the mean circulation in the Tasman Sea is an important problem to consider. The large-scale South Pacific gyre circulation is believed to be determined by the wind stress curl, Godfrey (1989) Island Rule and Sverdrup balance (Gray & Riser, 2014; Thomas et al., 2014). It is well documented (e.g., Kiss, 2010; Rhines & Schopp, 1991; Verron & Le Provost, 1991) that wind features (such as the steepest gradient in the integrated wind stress curl) offer at best a partial explanation for the separation latitude of western boundary currents (WBCs) due to the importance of advection in these regions. The reality in the climate change literature however, is that

linear theory and time-mean low-frequency changes in forcing are often used to attribute changes in WBC regions (e.g., Wu et al., 2012). Using observations (Maria Island temperature/salinity and XBTs) and two ocean state estimates, Hill et al. (2011) invoke steady state linear dynamics to associate changes in the basin-scale wind stress curl with the southern extent of the South Pacific gyre; they also found the EAC extension and Tasman Front transport to be anticorrelated. This wind-induced partitioning (also termed a "gating effect"; Ganachaud et al., 2014) of the EAC's pathway has been discussed by several subsequent studies on a range of time scales using both observations and models (e.g., Chiswell & Sutton, 2015; Hu et al., 2015; Oliver & Holbrook, 2014; Sloyan & O'Kane, 2015). Since subtropical gyres readily respond to low-frequency decadal wind forcing variability (Roemmich et al., 2016; Willebrand et al., 1980), existing work on the EAC gating effect has focused on low-frequency south Pacific basin-scale responses (Cai et al., 2005; Hill et al., 2011; Oliver & Holbrook, 2014); yet little is known about how the Tasman Sea circulation responds to local higher-frequency wind forcing.

There are a number of known factors that influence the East Australian Current's mean flow and variability. Due to the Indonesian Throughflow (Tomczak & Godfrey, 2003), the EAC has the weakest mean flow of the major WBCs (Mata et al., 2000, 2006; Tomczak & Godfrey, 2003); 22.1 Sv at 27°S (Sloyan et al., 2016). While the mean flow dominates the energy field at 27°S (Sloyan et al., 2016), at 30°S the energy field is increasingly eddy rich with the mean and standard deviation of transport being of a similar magnitude (Mata et al., 2000). The EAC exhibits a large seasonal cycle of 8.9 Sv at 27°S, with a narrower, higher transport (36.3 Sv) in Austral summer and a broader, weaker transport (27.4 Sv) during winter (Ridgway & Godfrey, 1997). Qiu and Chen (2004) observed that the EAC's seasonal cycle in EKE appears to be similar in amplitude and phase to the seasonal cycle of the south equatorial countercurrent. Subsequent studies Bowen et al. (2005) and Mata et al. (2006), focusing on mesoscale variability did not find strong evidence of offshore forcing. Recent work has implicated baroclinic Rossby waves in EAC transport variability at interannual to decadal time scales (Hill et al., 2008, 2011; Holbrook et al., 2011; O'Kane et al., 2014; Sloyan & O'Kane, 2015).

The growth, migration, and detachment of EAC eddies determines the EAC's separation latitude and are a large component of the transport in the EAC extension. Through the EAC's bifurcation and subsequent shedding process, the EAC spawns an eddy approximately every 100 days (Mata et al., 2006). A number of studies have attempted to understand the processes that cause the formation, detachment, and reattachment of mesoscale eddies in the separation region. Nilsson and Cresswell (1980) suggest a Rossby wave propagates westward along the Tasman Front to the separation region, reflecting off the coast, and subsequently pinching off eddies. Marchesiello and Middleton (2000), using a regional modeling configuration, corroborated the Nilsson and Cresswell (1980) eddy shedding process. In contrast, the contemporary view via observational and modeling studies (Bowen et al., 2005; Mata et al., 2006; Wilkin & Zhang, 2007) suggests eddies arise from locally generated mixed baroclinic and barotropic instabilities propagating southward along Australia's east coast with little involvement from Rossby waves at the eddy-shedding time scale. Although idealized models show that variable forcing can control the timing of intrinsic WBC variability (e.g., Kiss & Frankcombe, 2016), it remains an open question whether variable forcing can influence the timing of EAC eddy shedding or change the relative importance of barotropic/baroclinic instability in the EAC.

Past studies suggest that both barotropic and baroclinic instabilities are active in the EAC eddy shedding process; Bowen et al. (2005) and Mata et al. (2006) propose that barotropic energy conversion is the larger term in the separation region, although this dominance is not confirmed by Oliver et al. (2015). Future climate change simulations by Oliver et al. (2015) suggest that increases in both barotropic and baroclinic instabilities will drive increased growth and lifetime of anticyclonic eddies in the EAC extension, and this leads to a near doubling of eddy-related southward heat transport in the EAC extension. O'Kane et al. (2014) and Sloyan and O'Kane (2015) suggest that upstream EAC transport has not changed significantly in recent decades whereas increases in the EAC extension transport since 1948 are associated with propagating baroclinic disturbances across the South Equatorial Current into the East Australian Current. However, the Sloyan and O'Kane (2015) study was limited by a coarse 1° resolution which is unable to accurately resolve the EAC.

In summary, the EAC displays variability on a wide range of time scales; while the EAC appears to respond to low-frequency basin-scale variability and perhaps also local high-frequency forcing, the partitioning of variability in the EAC system between the intrinsic variability, and the response to these different forcings,

remains unknown. The focus of this study is to characterise the EAC's intrinsic variability and response in terms of both local and remote forcing. Specifically, this study will examine the influence of steady and variable forcing on the following:

1. the mean state of the EAC in terms of the partial separation, strength of EAC extension and Tasman sea circulation;
2. EAC eddy formation and shedding; and
3. the barotropic and baroclinic energy conversion in the EAC region.

Using the Nucleus for European Modelling of Ocean (NEMO) model, we present a hierarchy of eddy-permitting simulations beginning with steady forcing (no synoptic, seasonal, or interannual variability), and then introducing variability in the remote ocean boundaries, followed by atmospheric variability in the local Australasian domain, and finally full variability in both local and remote regions (see section 2.3 for discussion on the anticipated response). The experiments/model configuration is described in section 2 with model evaluation in section 3. Results characterizing the dominant role of the regional surface forcing in the rectified circulation in the Tasman Sea are given in sections 4.1–4.3 and a mechanism is proposed in section 4.4. Discussion and opportunities for further work are given in section 5.

2. Model and Methods

2.1. Ocean Model Configuration

The ocean general circulation model used in this study is version 3.4 of the Nucleus for European Modelling of Ocean (NEMO) model (Madec, 2012). NEMO solves the incompressible, Boussinesq, hydrostatic, primitive equations with a filtered free surface. NEMO uses a *z*-coordinate C-grid with partial cells at the bottom most layer in order to provide more realistic representation of bottom topography (Barnier et al., 2006). At the lateral continental boundaries, a free slip condition is employed which means that there is no velocity gradient (i.e., no horizontal shear) at the solid boundaries of the model. The energy-conserving and enstrophy-conserving momentum advection scheme and free slip configuration used have been found to be optimal for realistic variability of WBCs (Fransner, 2012; Le Sommer et al., 2009; Penduff et al., 2007). Topography is taken from the ETOPO1 data set (Amante & Eakins, 2009). In our configuration, NEMO has 75 vertical levels, with 24 levels in the upper 100 m and 22 levels between 100 and 1,000 m; this enables realistic representation of coastlines and continental shelves. This high number of near-surface levels also improves fidelity of the mixed-layer and thermocline variations (Bernie et al., 2005), as well as resolution of baroclinic flow (Stewart et al., 2017). NEMO is run with a prognostic turbulent kinetic energy (TKE) scheme for vertical mixing. Laterally we have spatially varying eddy coefficients (according to local mesh size) with a Laplacian operator for iso-neutral diffusion of tracers and a biharmonic operator for lateral diffusion of momentum.

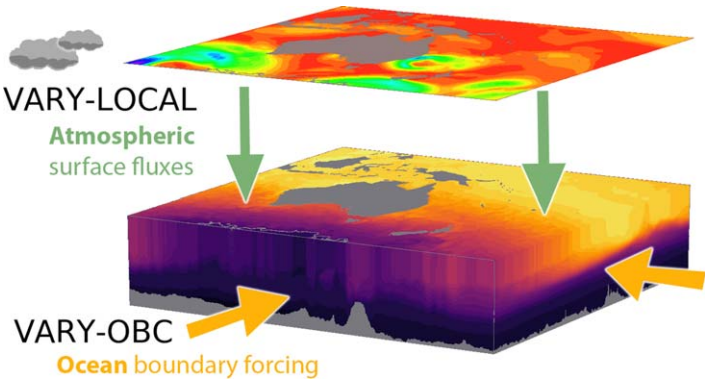

Figure 1. Experiment design schematic that illustrates the model domain and spatial extent of the variable forcing. (bottom) NEMO configuration has a regional domain (pictured) that is forced by ERA-Interim at the surface and ORCA025-L75-MJM95 in the ocean boundaries. The four main experiments consist of (1) steady surface forcing and ocean boundary conditions (CONSTANT), (2) varying the remote ocean (VARY-OBC), (3) varying surface fluxes (VARY-LOCAL), and (4) varying both the remote ocean and local forcing (VARY-ALL). Fields are illustrative only, pictured are snapshots (14 May 2005) of the (top) variable surface wind stress and (bottom) temperature.

The regional Australasian model domain is pictured in Figure 1. The grid is curvilinear (shown in Figure 2) with an eddy-permitting (nominally 1/4°) horizontal resolution. Specifically, the meridional width of each grid cell is 24.5 km whereas the zonal width varies with both longitude and latitude between 19.5 and 24.5 km. This regional simulation is forced by temperature, salinity, *u*/*v*-velocity at the open ocean boundaries with 5 day means from a global NEMO ocean simulation run at 1/4° resolution with 75 vertical levels (namely, ORCA025-L75-MJM95, provided by the DRAKKAR/MyOcean group; Barnier et al., 2007, 2011). Further details regarding the handling of the ocean boundary conditions are given in Madec (2012, section 8.4), Barnier et al. (1998), and Marchesiello et al. (2001). ORCA025-L75-MJM95 was forced by the 3-hourly T255 (∼0.75°) ERA-Interim atmospheric reanalysis (Dee et al., 2011) through the CORE bulk formulae. The initial conditions for ocean temperature and salinity are taken from Levitus et al. (1998) with an ocean at rest. The regional simulation surface forcing is also from the ERA-Interim atmospheric reanalysis (Dee et al., 2011) between 1989 and 2009. There is no sea surface salinity relaxation in

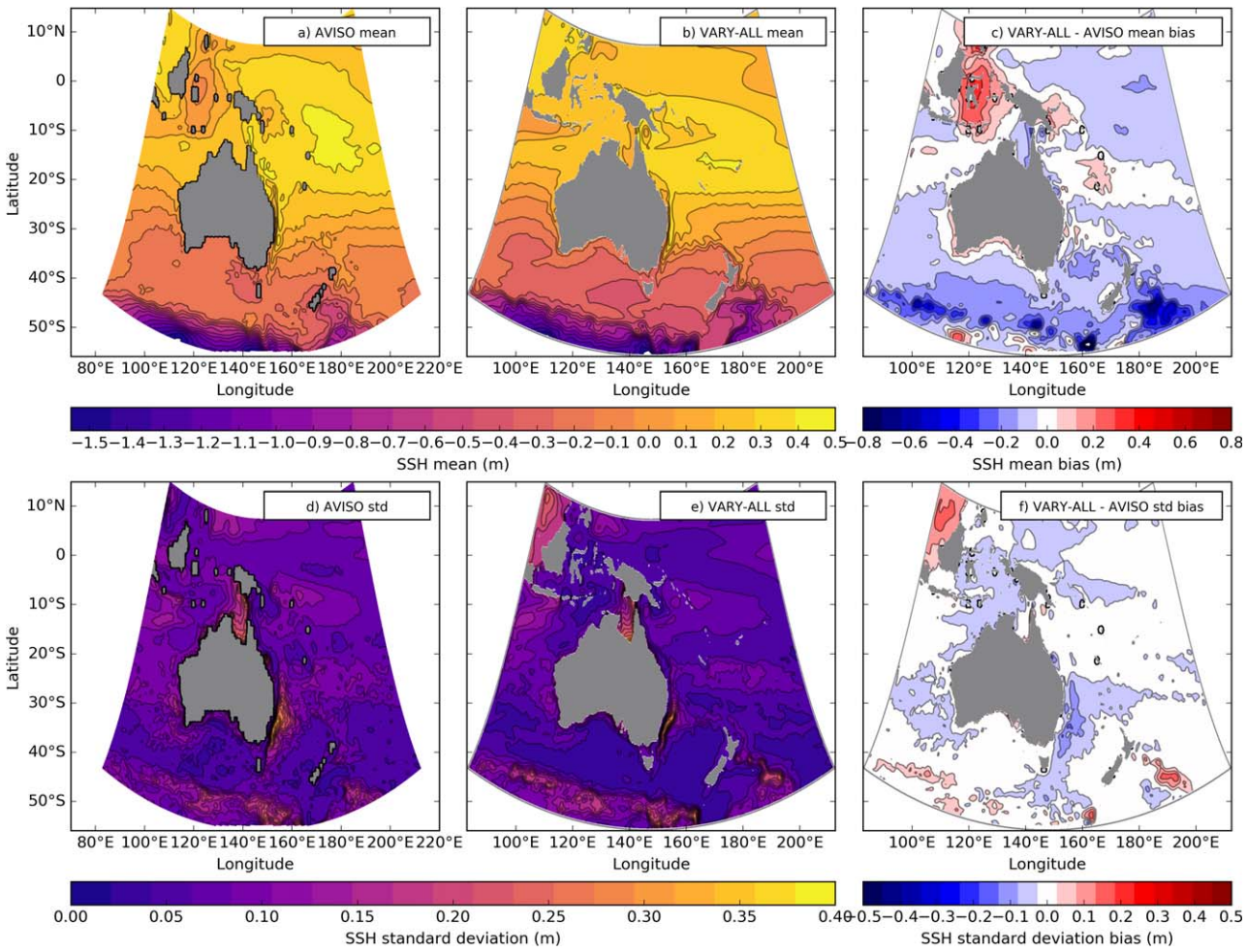

Figure 2. Comparison of VARY-ALL (NEMO) and AVISO sea surface height (SSH) between 1994 and 2009. (a, b) Mean SSH anomaly and (d, e) SSH standard deviation. The sea surface height mean anomalies in Figures 2a and 2b are relative to the temporal and spatial average to emphasise the difference in time-mean gradients between VARY-ALL and AVISO. Biases of VARY-ALL relative to AVISO are given in Figures 2c and 2f.

the regional domain; precipitation plus runoff minus evaporation determines the freshwater flux across the air-sea interface. The temporal resolution of ERA-Interim in the regional domain depends on the variable: winds and humidity are imposed at 3-hourly time steps whereas precipitation and longwave/shortwave radiation are imposed daily. Our simulations are analyzed from 1994 to 2009, in which ERA-Interim uses data from continuous satellite wind stress coverage, namely, ERS-1, ERS-2, and QuickSCAT (Dee et al., 2011).

2.2. Experiments

The ERA-Interim variables within the Australasian domain will be referred to as the *local forcing* and the ocean boundary conditions (OBCs; taken from the ORCA025-L75-MJM95 simulation) will be called the *remote forcing*. All experiments have the same time-mean local and remote boundary forcing.

The four main experiments used to assess the impact of local and remote forcing variability on the Tasman Sea circulation are as follows:

1. CONSTANT has no local or remote forcing variability (all forcing fields, both local and remote taken from the 21 year time-mean fields);
2. VARY-OBC has a constant time-mean local forcing but varying remote ocean boundary conditions (5 days to interannual time scales in temperature, salinity, and velocity);
3. VARY-LOCAL has a constant remote forcing but varying local surface atmospheric forcing over the regional domain (3-hourly averages for winds and humidity, through to daily, seasonal and interannual time scales for those and all other variables); and

4. VARY-ALL has both local and remote forcing variability (i.e., VARY-LOCAL and VARY-OBC).

A schematic of the model experiment design in terms of the VARY-LOCAL and VARY-OBC forcing locations is pictured in Figure 1. All experiments are shown in supporting information Table S1.

In contrast to idealized studies (Andres et al., 2012; Jouanno et al., 2016; Pedlosky, 1965; Veronis, 1970; Willebrand et al., 1980), the experiments here utilize realistic bathymetry, coastlines, stratification, and nonstationary/nonhomogeneity in the wind stress fields. The novelty of these experiments is that they progress from an idealized time-mean steady forcing to a fully varying realistic configuration (i.e., VARY-ALL) that would be typical of the oceanic component of a CMIP model.

In the variable local forcing cases, taking the time-mean of the wind velocity field would result in different time-mean wind *stress* fields, due to the quadratic dependence of the wind stress on the wind velocity (e.g., Zhai, 2013) and nonlinear terms in the calculation of the drag coefficient (Large & Yeager, 2004). As the focus of this study is the nonlinear EAC response to variable forcing, this issue is best avoided. Therefore, the NEMO simulations described above are run with directly prescribed air-sea fluxes (including heat, freshwater and stress) in the regional domain. To obtain the fluxes and minimise temperature and salinity drift, NEMO was first run with fully varying ERA-Interim fluxes using the CORE bulk formulae with absolute wind (Large & Yeager, 2004), and the resulting 3-hourly surface stress, freshwater, and heat fluxes were stored and used to force all the above NEMO simulations (including VARY-ALL), using the time-mean where described. This approach ensures that the time-mean of all components of air-sea fluxes to be the same across all the experiments, regardless of the variability imposed in the forcing.

Another five experiments are used to determine which wind frequencies in the local wind stress forcing are responsible for the changes we see in the mean circulation (see section 4). These have fixed lateral boundary conditions as in VARY-LOCAL, and all surface fluxes except for the wind stress are also fixed. The wind stress field in the local domain (used to force VARY-LOCAL and VARY-ALL) contains variability from 3-hourly to interannual time scales. In experiments 5–9, we high pass, low pass, or band pass the wind stress via various "brick wall" filters in the frequency domain, yielding five experiments forced by variability restricted to (5) $<$56 days, (6) 56–148 days, (7) 148–330 days, (8) 330–400 days, and (9) $>$400 days period. The time-mean wind stress from the unfiltered forcing is also added to the filtered forcing in experiments 5–8 so that all five experiments include the same time-mean. Experiment 5 is intended to capture synoptic to monthly variability with experiments 6–9 capturing progressively longer modes of variability. In particular, experiment 8 contains the annual peak and experiment 9 has interannual and longer variability. Our approach of filtering the wind field in frequency space is different from the monthly averaging of atmospheric variables (e.g., Penduff et al., 2011; Wu et al., 2016), the latter method would be similar to a $<$400 day experiment (not experiment 8).

Similar to other boundary current regional configurations (e.g., Renault et al., 2016b), experiments are spun-up for 5 years (in this case January 1989 to December 1993; see supporting information Figure S1), and all results presented in this study use daily-averaged model output from 16 years of integration after spin-up (January 1994 to December 2009).

2.3. Theoretical Expectations: Anticipated Response to Varying Forcing

The anticipated EAC response from steady to realistically varying forcing warrants an a priori discussion, in which we also define some necessary terminology. We define *intrinsic variability* as variability arising without any variability in the local surface forcing or remote ocean boundary conditions. This terminology differs from some studies, for example Sérazin et al. (2015) who define intrinsic variability as ocean variability arising from an atmospheric forcing with a repeated climatological seasonal cycle. *Rectification* is defined as the emergence of a different time-mean state (despite the same time-mean forcing) due to variability in the atmosphere or ocean boundary conditions. Oceanic variability is a result of a combination of (1) the response of the ocean to local and/or remote forcing variability and (2) intrinsic dynamical instability processes (e.g., barotropic/baroclinic instability, or topographically generated eddies and meanders in oceanic jets; Stammer & Wunsch, 1999). On the large scale, the time-mean wind stress alone is expected to drive an oceanic circulation characterised by an intense WBC that is intrinsically unstable (e.g., Pedlosky, 1996). The wind field's fluctuating component alone can also give rise to rectified mean currents, that are likely much weaker in magnitude (Willebrand et al., 1980). The subsequent mean and rectified mean currents from the

mean and variable winds interact to create a new mean circulation. To put this in context, the CONSTANT experiment will only have mean currents from the mean forcing whereas the VARY-LOCAL simulation will have the net interaction of time-mean currents from the time-mean and variable forcing. While the difference between the VARY-LOCAL and CONSTANT simulations will allow us to infer the effect of local variable forcing, this study will not characterise the rectified mean circulation from variable forcing with zero mean. Similar approaches to understanding the effect of variable forcing are used in Penduff et al. (2011) and Jouanno et al. (2016).

2.4. Estimating the Separation Latitude

The separation latitude of the EAC is calculated from each daily average output, using SSH contours to indicate a separation of the main current from the coast, following the method described by (Cetina-Heredia et al., 2014; Ypma et al., 2016). This method captures eddy detachment and reattachment, which characterises changes in the separation latitude on short time scales. The method involves the following:

1. Finding the core of the EAC upstream of the separation at 28°S, defined as the maximum southward geostrophic surface velocity as determined from the SSH field.
2. Following the SSH contour at the location of the maximum velocity southward, and then recording the first location at which the contour turns more than 30°S eastward of south as the separation latitude.

Daily separation latitudes lying more than 1 standard deviation from the 50 day running mean are considered false detections and ignored (gray crosses in Figure 7).

2.5. Eddy Tracking

This study uses the eddy detection and tracking algorithm developed by Chelton et al. (2011) and coded by Oliver et al. (2013). Eddy detection involves finding closed contours of sea level anomalies above a specified threshold for each daily map of filtered sea surface height. Additional necessary criteria include: a minimum eddy radius, peak amplitude and local extrema for cyclonic and anticyclonic eddies. Eddy tracks are then generated for each eddy by searching for all eddy centroids at successive time steps that lie within a specified ellipsoid centred on the eddy. Further details of the algorithm can be found in Chelton et al. (2011, Appendix B2) and its implementation can be found in Oliver et al. (2013, Appendix A).

2.6. Energetics

Energetics metrics are used to quantify differences in the energy conversion between the experiments. Here we define the eddy state as any deviation from the time-mean state; this results in a Reynolds decomposition of the zonal (u) and meridional (v) velocities into their time-mean ($\overline{u}$, $\overline{v}$) and eddy-varying components (u', v'), and similarly for density ρ. We calculate the following widely used (e.g., Bowen et al., 2005; Eden & Böning, 2002; Loveday et al., 2014; Mata et al., 2006; Oliver et al., 2015) quantities (all averaged between depths z_1 and z_2):

1. Mean kinetic energy,

$$\mathrm{MKE}(x,y)=\frac{\rho_0}{2(z_2-z_1)}\int_{-z_2}^{-z_1}\left(\overline{u}^2+\overline{v}^2\right)dz; \tag{1}$$

2. Eddy kinetic energy,

$$\mathrm{EKE}(x,y)=\frac{\rho_0}{2(z_2-z_1)}\int_{-z_2}^{-z_1}\left(\overline{u'^2}+\overline{v'^2}\right)dz; \tag{2}$$

3. Mean potential energy → eddy potential energy (MPE→EPE),

$$\mathrm{BCC}=\frac{g}{z_2-z_1}\int_{-z_2}^{-z_1}\left(\frac{\overline{u'\rho'}\ \frac{\partial\overline{\rho}}{\partial x}+\overline{v'\rho'}\ \frac{\partial\overline{\rho}}{\partial y}}{\frac{\partial\overline{\rho}}{\partial z}}\right)dz; \tag{3}$$

4. MKE → EKE is

$$\mathrm{BTC} = -\frac{\tilde{\rho}}{z_2 - z_1}\int_{-z_2}^{-z_1}\left(\overline{u'u'}\frac{\partial \overline{u}}{\partial x} + \overline{u'v'}\left(\frac{\partial \overline{u}}{\partial y} + \frac{\partial \overline{v}}{\partial x}\right) + \overline{v'v'}\ \frac{\partial \overline{v}}{\partial y}\right)dz. \tag{4}$$

Physically, positive values of equation (3) are an indication of baroclinic instability (BCC) and positive values of equation (4) suggests the occurrence of barotropic instability (BTC). Since $z_2 - z_1$ is the thickness of each latitude/longitude grid cell, the depth average removes the effects of topography/partial cells. The kinetic energy is based on $\rho_0 = 1,035\ \mathrm{kg\ m^{-3}}$, as that is the value used in NEMO in solving the momentum equations under the Boussinesq approximation. Density for BCC and BTC was calculated from the temperature and salinity fields using the Jackett and McDougall (1994) Equation of State which matches the method used in this version of NEMO. Reference stratification $\tilde{\rho}(z)$ is approximated by the zonally and meridionally averaged density; see Kang and Curchitser (2015, Appendix) for a discussion of the sensitivity to the reference stratification. Typical of other studies using these metrics (e.g., Böning & Budich, 1992; Haidvogel & Beckmann, 1999; Mata et al., 2006), contributions from vertical velocities are likely small and so are neglected. Similarly, these diagnostics are calculated offline from daily average fields where ensemble averaging simplifies the computation, e.g., $\overline{u'u'} = \overline{uu} - \overline{u}\,\overline{u}$ (Doddridge et al., 2016; Stewart et al., 2015).

3. Evaluation of the Simulated Tasman Sea Circulation (VARY-ALL)

3.1. Mean and Variability of Sea Surface Height

In Figure 2, the VARY-ALL simulation with full variability is evaluated with respect to satellite altimetry (AVISO) over 1994–2009 when the available observations and simulation overlap. The VARY-ALL Tasman Sea large-scale circulation is similar to the observations; specifically, the East Australian Current and East Auckland Current are clearly visible in VARY-ALL. In particular, the EAC's modeled SSH gradients are similar in location and structure. Biases however do exist (Figure 2c); for example, there are SSH gradients in the Indonesian Throughflow that are not present in VARY-ALL and the modeled SSH gradients across the Tasman Front are sharper than the observations. The Antarctic Circumpolar Current region has biases in the location and strength of fronts along the southern edge of the domain, particularly in Figure 2c. These biases may be related to the ORCA025-L75-MJM95 ocean boundary conditions, limited fidelity in the resolved bathymetry and the relatively coarse resolution of the model configuration (since the Rossby radius decreases as latitude increases).

The variability of sea surface height in VARY-ALL is also in good agreement with AVISO in many areas (see white areas in Figure 2f) but underestimated by up to 50% in the East Australian Current (Figures 2d–2f). This underestimation is typical of 1/4° eddy-permitting resolution models (e.g., Ypma et al., 2016). There is also an enhancement of variability in the north-western corner of the domain, which is largely an artefact of running a regional simulation in which equatorially trapped waves cannot exit the domain. Given that this spurious variability is far away from our region of interest it is unlikely to adversely affect the results presented.

3.2. Depth-Integrated Transports in the East Australian Current Region

Depth-integrated time-mean (1994–2009) transports down to 1,945 m in VARY-ALL and observations in the Tasman Sea are shown in Figure 3. These section locations and observations are also analyzed in Oliver and Holbrook (2014). Section end points match those of Oliver and Holbrook (2014), insofar as the model grid allows, to ensure a closed transport budget. The observations originate from Ridgway and Godfrey (1994) and Ridgway and Dunn (2003) (RG94) and the CSIRO Atlas of Regional Seas (CARS) climatology (Ridgway et al., 2002) using a reference level of 2,000 dbar (level of no motion). The VARY-ALL (NEMO), MOM, OFAM, and RG94 transports include both Ekman and geostrophic components, but the CARS transports are geostrophic components only. From Oliver and Holbrook (2014, Figure 5), for RG94, the Ekman components for sections FE, ED, DG, AB are 0–12% of the RG94 geostrophic transport and 100% for BC, thus aside from BC, we can expect the omission of the Ekman component in CARS would have only a small effect on the results presented.

Comparing transports flowing into the boxed Tasman Sea region to observations, the VARY-ALL simulation approximately captures the core EAC transport (FE) but overestimates the southern inflow (BC). Across BC,

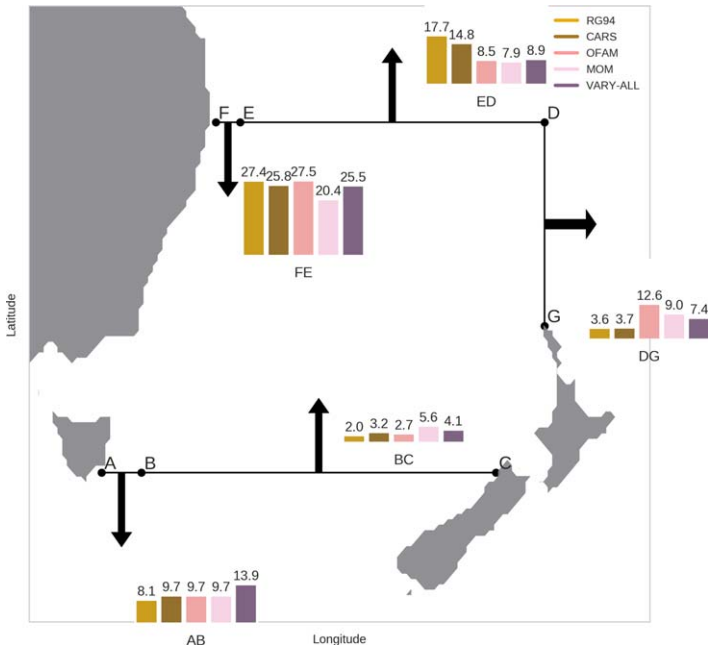

Figure 3. Schematic of VARY-ALL (NEMO) mean depth-integrated transport with observations (browns) and models (pinks). Units are Sverdrups. NEMO transports are depth-integrated to 1,945 m. The observations are from Ridgway and Godfrey (1994) (RG94) and CARS, via Oliver and Holbrook (2014). Model transports OFAM and MOM are from Oliver and Holbrook (2014) and Ypma et al. (2016), respectively. Section end points are similar to Oliver and Holbrook (2014) but sections are aligned with the curvilinear model grid (not strictly zonal/meridional); transport is calculated using grid, normal velocities. The section end points are (A) 148.2°E, 42.6°S, (B) 150.8°E, 42.6°S, (C) 172.5°E, 40.6°S, (D) 171.3°E, 25.8°S, (E) 155.6°E, 27.6°S, (F) 153.6°E, 27.8°S, (G) 173.6°E, 34.9°S, (H) 146.9°E, 43.4°S, and (I) 146.9°E, 45.8°S.

given that the observed geostrophic transport varies by 2.2 Sv (1.0 Sv in RG94 versus 3.2 Sv in CARS), the bias in the VARY-ALL simulation is small. The modeled upstream EAC transport (FE) of 25.5 Sv is within the observed and modeled range of EAC transports shown in Figure 3, and most importantly the recent 18 month full-depth 152 km wide mooring based observations by Sloyan et al. (2016) at 27°S, namely 22.1 ± 7.5 Sv.

Examining transports out of the Tasman Sea box, we see a weaker northward outflow (ED) compensated by anomalously strong eastward outflows (DG) and the EAC extension (AB). Comparing combined north-eastward outflow (DG + ED), VARY-ALL (16.2 Sv) and MOM (16.9 Sv) simulate a weaker DG + ED outflow than is observed by RG94 (21.3 Sv) and CARS (18.5 Sv). Having said this, while not directly comparable to DG, more recent, direct mooring observations of the Tasman Front in the Tasman Sea interior give a higher mean transport of 7.8 Sv (Sutton & Bowen, 2014) with high variability ranging between −4 and 17.8 Sv (4.4 Sv standard deviation). The VARY-ALL simulation's large bias in the EAC extension (AB) is likely offset by having the weakest north-eastward outflow at DG + ED as well as the previously discussed stronger inflow across BC.

In summary, while biases in transport magnitude remain, the VARY-ALL simulation captures the overall structure and magnitude of Tasman Sea circulation.

4. Results

Throughout this paper, the CONSTANT experiment is used as a control because it is the shared basis of all nine experiments (see section 2.2 or supporting information Table S1) and also enables a characterization of changes in the mean and variable state of the Tasman Sea circulation that are not intrinsic to the mean forcing.

4.1. Sea Surface Height and Transport Comparison

Spatial maps of NEMO sea surface height mean and standard deviation anomalies under differing forcing are presented in Figure 4. In the Tasman Sea, VARY-ALL more closely resembles VARY-LOCAL than VARY-OBC in the changes of SSH mean and standard deviation relative to CONSTANT. Assuming the forcing effects are linear, this suggests that the local surface forcing is largely responsible for the spatial pattern of change seen in VARY-ALL in the Tasman Sea.

Focusing on the time-mean changes from CONSTANT in Figures 4b–4d, VARY-LOCAL and VARY-ALL have the largest changes in the Tasman Sea circulation, with a less distinct Tasman Front and a more defined EAC extension (clearest in Figures 4c and 5a). The standard deviation of sea surface height (Figures 4f–4h) shows the spatial changes in variability between the experiments with forced variability and CONSTANT. VARY-OBC shows a basin-wide increase in variability and a relatively small reduction in eddy activity in the EAC extension. In both the VARY-LOCAL and VARY-ALL (Figures 4g and 4h) simulations, there is a large reduction in variability in the EAC separation region, and also an increase in variability in both the upstream region of the EAC and the EAC extension. Ypma et al. (2016) also find enhancement of variability both upstream and in the EAC extension when changing from atmospheric normal year forcing to forcing with full interannual variability (their Figures 3c and 3d); however, unlike Figures 4g and 4h, they additionally found enhanced variability in the separation region.

The dramatic change in mean SSH gradients between CONSTANT and VARY-LOCAL in the EAC separation region can be visualised more clearly using a barotropic streamfunction (Figure 5a). The Tasman Sea-wide shift seen in the VARY-LOCAL experiment in Figure 4c, is now more clearly visualised as an overall increase in transport across the Tasman Sea with the largest depth-integrated increases in transport in the EAC

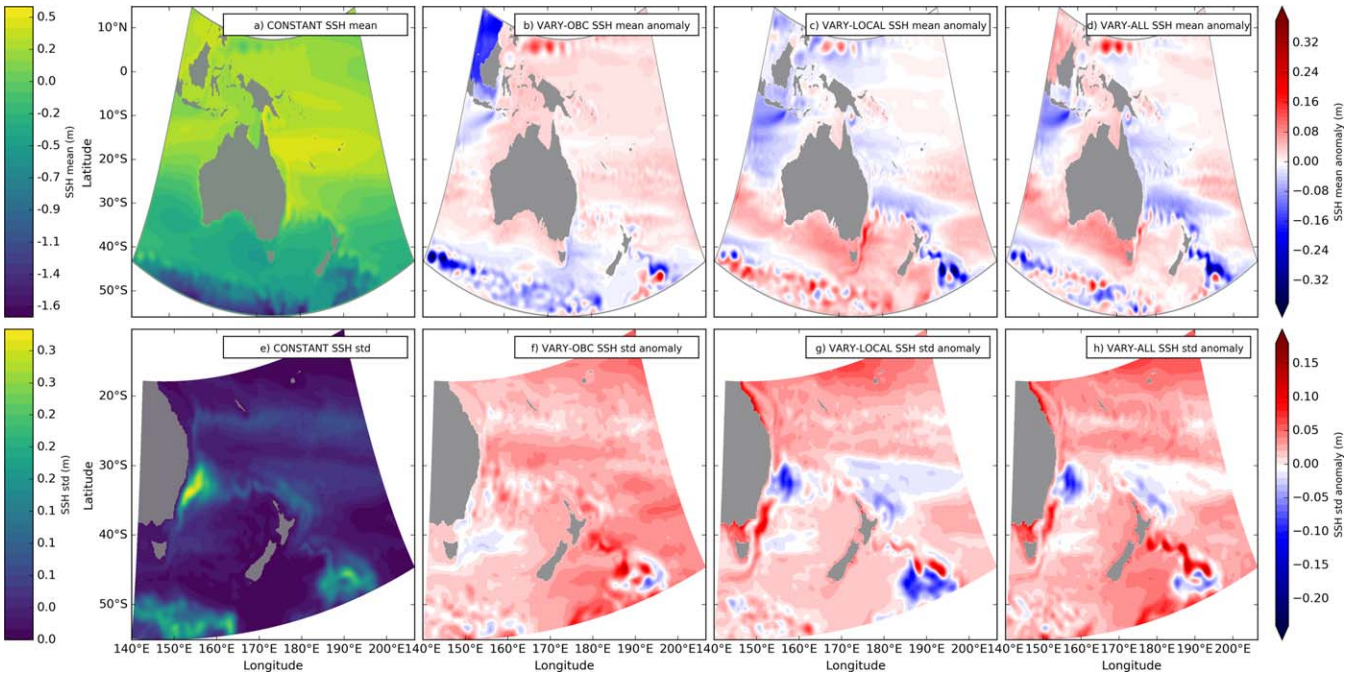

Figure 4. (a) Sea surface height (m) and (e) its standard deviation (m) for the CONSTANT (control) experiment. (b–d) SSH anomaly relative to CONSTANT for VARY-OBC, VARY-LOCAL, and VARY-ALL, respectively (to emphasise the changes in the geostrophic currents between each experiment, the area-mean is removed from each sea surface height field). (f–h) SSH standard deviation anomaly relative to CONSTANT for VARY-OBC, VARY-LOCAL, and VARY-ALL, respectively. Positive anomalies indicate values exceed CONSTANT.

extension along the coast of Australia. The depth-integrated transports in Figure 5b corroborate this story, indicating that the variability in the local surface forcing (VARY-LOCAL) increases the proportion of mean EAC transport that flows into the EAC extension (section JK), with a concomitant reduction in the transport in the Tasman Front (section GD).

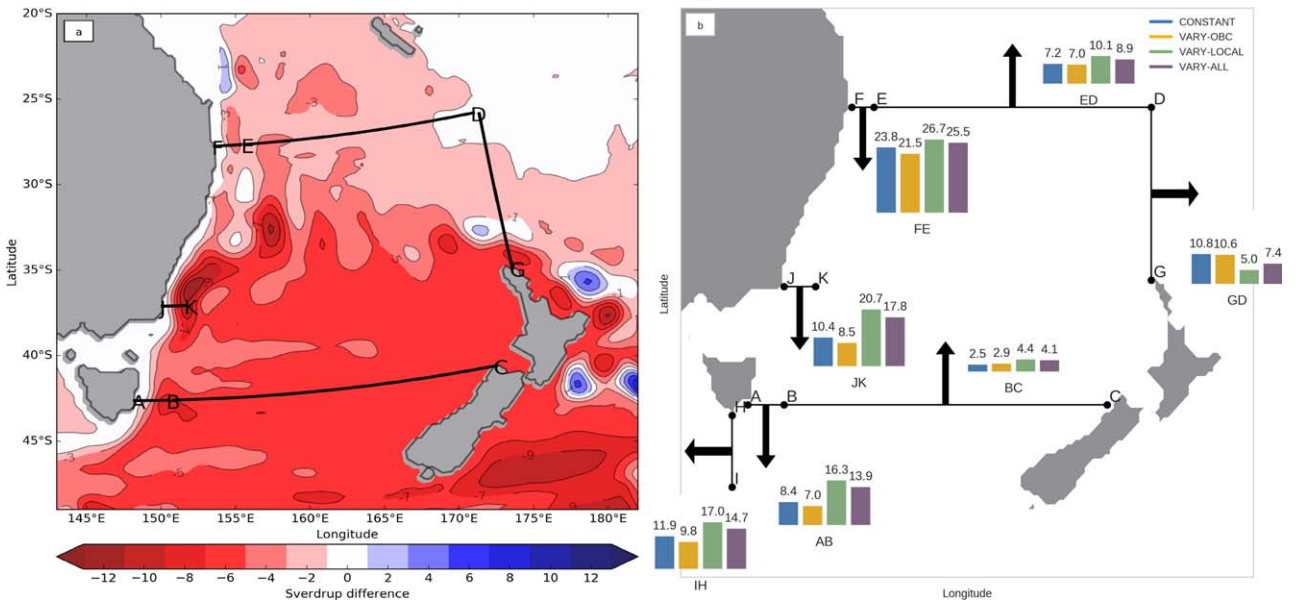

Figure 5. (a) Time-mean barotropic streamfunction difference between VARY-LOCAL and CONSTANT (integration taken eastward from Australia down to 1,945 m; contours every 2 Sv), red (blue) indicates areas of enhanced (reduced) transport when local surface forcing is introduced. (b) Comparison of depth-integrated transport (Sv) to 1,945 m between CONSTANT (blue), VARY-OBC (yellow), VARY-LOCAL (green), and VARY-ALL (lavender). The section end points are the same as Figure 3, with the addition of points J (150.1°E, 37.1°S) and K (151.7°E, 37.1°S).

Figure 5b quantifies the effect of variable forcing on the time-mean Tasman Sea circulation. Across all coastal sections and experiments, the EAC postseparation (JK) displays the largest range of transports (8.5–20.7 Sv). Despite a modest mean change in upstream EAC transport (FE), we see a large rectification response at JK of 10.3 Sv between CONSTANT and VARY-LOCAL down to 1,945 m (standard error in the mean at JK is 0.7 and 1.6 Sv, respectively). Across all sections excluding GD and BC, relative to the steady state forcing in CONSTANT we find that variability in the remote ocean (VARY-OBC) weakens mean transport; for all sections excluding GD, variability in both the local/remote forcing (VARY-ALL) increases transport, and variability in the local forcing alone (VARY-LOCAL) produces the largest mean transport. The calculated net transport into the Tasman Sea bounded by A-F is 0.2–0.5 Sv for the four experiments, smaller than the imbalances of 0.5 ± 2, -0.8, 0.6, and 1.5 Sv in Ridgway and Godfrey (1994), CARS, Ypma et al. (2016) and Oliver and Holbrook (2014), respectively. Interestingly, since all four experiments feel the same time-mean wind stress curl, a steady state linear Sverdrup-Island Rule (Godfrey, 1989; Sverdrup, 1947) model would give the same transport across GD, whereas our model gives a wide range of Tasman Sea outflow transports, from 5 to 10.8 Sv. Before proposing a mechanism for the described rectified circulation (section 6.4), we first examine changes in EAC variability.

4.2. Changes in EAC Transport Variability

We now explore how changes in transport variability determine the different mean states discussed in section 4.1. To this end, Figure 6 shows power spectra, violin plots and boxplots for coastal EAC sections (FE/

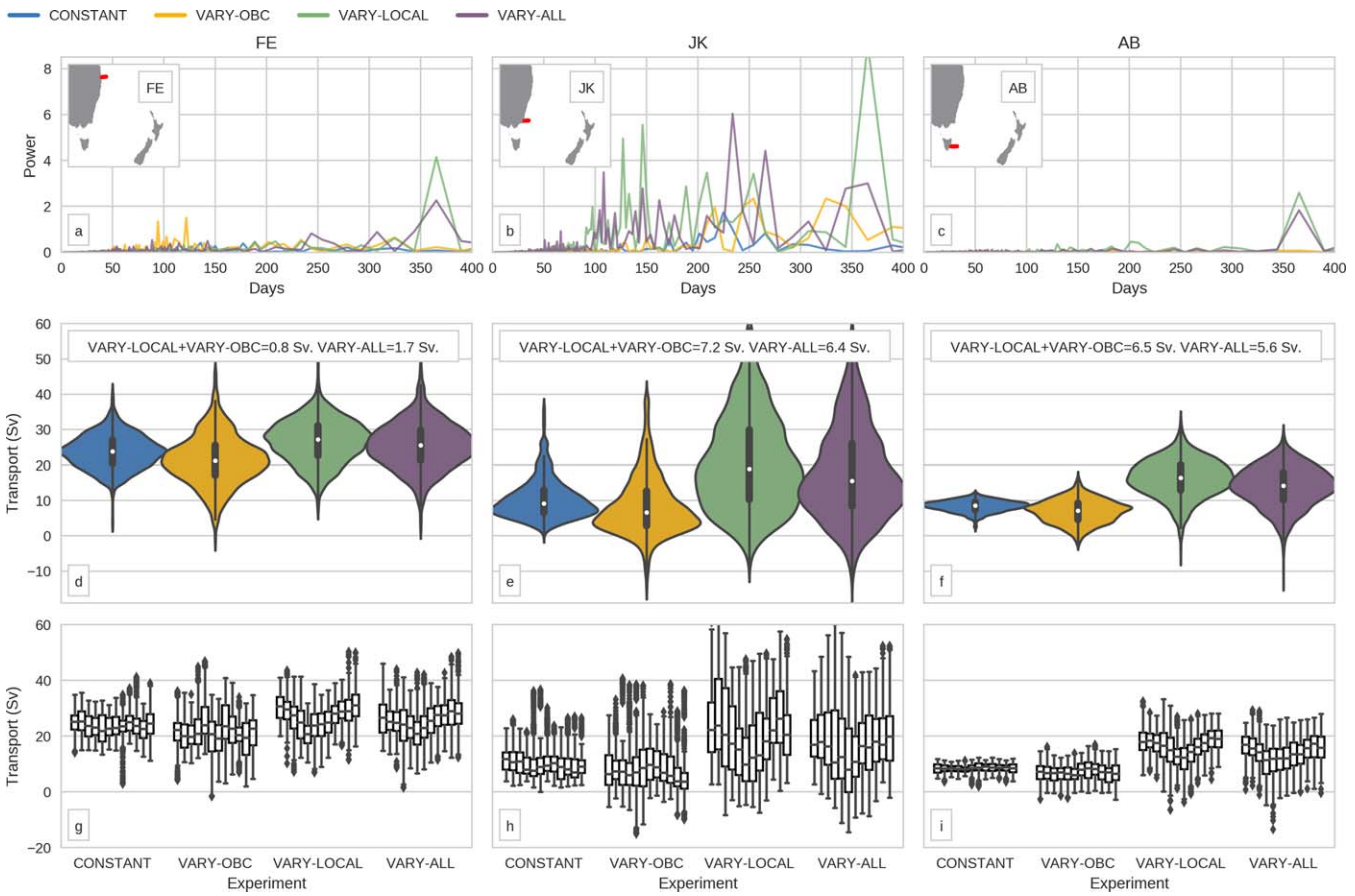

Figure 6. Comparison of depth-integrated (to 1,945 m) southward transport time series in terms of (a–c) power spectra, (d–f) violin plots, and (g–i) box plots for each month January–December, where each column is a different transport section across FE/JK/AB (see inset in Figures 6a–6c for location of section) for the four experiments (CONSTANT/VARY-OBC/VARY-LOCAL/VARY-ALL). The violin plots contain a normal box plot with the additional "violin" indicating the transport distribution through a kernel density estimate (Scott reference rule is used for bandwidth selection). The top and bottom of each box (Figures 6d–6i) indicate the interquartile range (IQR). The median is represented by a white dot (Figures 6d–6f) or the mark within the box (Figures 6g–6i). The whiskers in Figures 6d–6i extend 1.5 $\times$ IQR beyond the box; dots that fall outside the whiskers (Figures 6g–6i only) are thus considered outliers. The textboxes in Figures 6d–6f check the linearity of the response in terms of median transport anomaly relative to CONSTANT.

JK/AB) for the four experiments. Figure 6d shows that the upstream EAC has large intrinsic variability with CONSTANT the least variable and VARY-OBC the most variable. Specifically, Figure 6d shows that the CONSTANT EAC upstream (FE) interquartile range (IQR) of transport is 6.5 Sv; the remaining experiments have a larger IQR $\sim$ 8.5 Sv. The upstream EAC transport (FE) standard deviation for CONSTANT (4.8 Sv) is a sizeable fraction of that for VARY-OBC, VARY-LOCAL, and VARY-ALL (7.1, 6.1, and 6.5 Sv, respectively). These values are similar to the EAC transport standard deviation of 7.5 Sv found by Sloyan et al. (2016) in an 18 month full-depth 152 km wide mooring at 27°S. Comparing to CONSTANT, the increased IQR of VARY-OBC at JK and AB corroborates work by Hill et al. (2010), suggesting remote oceanic variability affects EAC extension transport variability.

The period with the greatest power in the power spectra (Figures 6a–6c) is the annual peak at 365 days in the VARY-LOCAL experiment. A suggestion of seasonality is shown in the boxplots for the VARY-LOCAL and VARY-ALL experiments at FE and AB (Figures 6g and 6i). At FE, this is likely the documented summertime peak in upstream EAC transport (Ridgway & Godfrey, 1997; Wang et al., 2013). It is notable that remote forcing appears to play little role in the seasonality of the upstream EAC (VARY-OBC, Figure 6a). In all sections (Figures 6a–6c), VARY-ALL appears to have a weaker annual peak compared to VARY-LOCAL, suggesting that the varying ocean boundary conditions are dampening the annual signal. Section JK is interesting as there are peaks for VARY-LOCAL/VARY-ALL between 90 and 200 days, some with a similar magnitude to the annual peak. This variability is likely related to the documented EAC eddy-shedding time scale (Bowen et al., 2005; Mata et al., 2000, 2006; 90–180, 90–140, $\sim$100 days, respectively) and will be examined more closely in the next section.

4.3. Changes in Eddy Shedding and the EAC Separation Latitude

Time series of the separation latitude (details in section 2.4) for the four experiments are presented in Figure 7. The separation latitude in the experiments including local forcing variability (i.e., VARY-LOCAL/VARY-ALL) is consistently further south. The mean separation latitude shift of 0.7°S (supporting information Figure S2) between CONSTANT and VARY-LOCAL exceeds the standard error in these means (0.1° in both cases), indicating that the mean separation change is statistically significant despite being small relative to

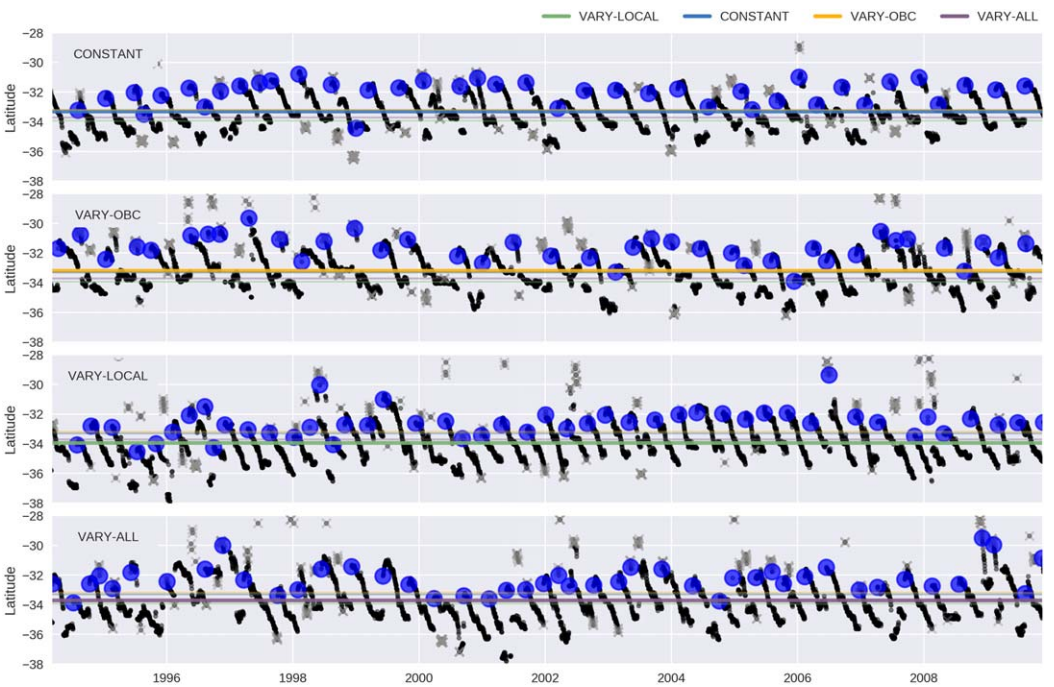

Figure 7. Separation latitude time series comparison. Black dots are detected separation latitude (gray crosses are considered false-positive outputs by the separation latitude algorithm). A "retraction event" (blue circles) is defined as the times when the separation latitude jumps northward by more than 1.5° in a single day. Separation latitude mean is indicated for all experiments by horizontal lines.

the variability. Moreover, the 0.7°S EAC separation shift is similar to the increase in mean separation latitude found in recent eddy-resolving simulations applying trends in forcing. For example, Oliver and Holbrook (2014) found a 0.8°S shift from present to future climate in a ∼60 year A1B climate change scenario and Cetina-Heredia et al. (2014) found a modeled 67 km poleward mean shift during 1980–2010. The implications of this result will be discussed further in section 5.

The introduction of variability in the local surface forcing decreases the time between eddy shedding events. There are 41, 40, 49, and 45 detected retraction events (blue circles) in CONSTANT, VARY-OBC, VARY-LOCAL, and VARY-ALL, respectively. While the variability in retraction period is high (supporting information Figure S3), the introduction of regional atmospheric variability (VARY-LOCAL) leads to a 15% decrease in the mean time between eddy shedding events as compared to the intrinsic EAC eddy shedding time scale (CONSTANT). This change is statistically significant relative to the standard error in the mean. Given the increase in variability in the postseparated EAC in VARY-LOCAL in Figure 6e, it is notable that the EAC retraction period's IQR is smallest (i.e., the shedding is most regular) with regional atmospheric variability (VARY-LOCAL), suggesting that the annual cycle in the local forcing (see Figure 11f) may play some role in the timing of eddy shedding.

4.4. Dynamics of Rectified Tasman Sea Circulation

Since we have now established that the variability in EAC extension is mostly attributable to variability in the local atmospheric forcing, the remainder of section 4 will focus on the differences between the CONSTANT and VARY-LOCAL experiments.

Figure 8 shows large-scale changes in the eddy kinetic energy (EKE) field at the surface (0–200 m) and changes in the mean kinetic energy field (MKE) at the surface and at depth (200–1,945 m) with the introduction of local variability. Near-surface MKE is increased in the EAC extension region but generally reduced upstream in the EAC, the EAC separation region, Tasman Front and offshore in the South Caledonian jet. In contrast, the response below 200 m is a consistent enhancement of MKE along the coast. Stronger MKE at depth is consistent with an enhanced EAC extension (Figure 5a) and the idea that water parcels below approximately 460 m are more likely to end up in the EAC extension (Ypma et al., 2016). Figure 8c shows a broad enhancement of near-surface EKE across the Pacific north of 25°S, with a strong increase in upstream coastal EKE up to Papua New Guinea. An increase in EKE south of New Caledonia also appears in VARY-LOCAL. Strong surface EKE south of New Caledonia can be seen in AVISO (Qiu & Chen, 2004), ORCA-R025 (Barnier et al., 2006), and OFAM3 also forced by ERAI (Feng et al., 2016). Additionally, there is a large reduction in EKE in the upstream offshore area/separation region (25°S–35°S, 150°E–160°E) and a large increase in EKE in the EAC extension region (35°S–42°S, ∼153°E). EKE differences below 200 m (not shown) are similar to Figure 8c. In summary, when the local surface forcing varies, the near-surface EKE in the upstream EAC and subsurface MKE along the pathway of the EAC is enhanced.

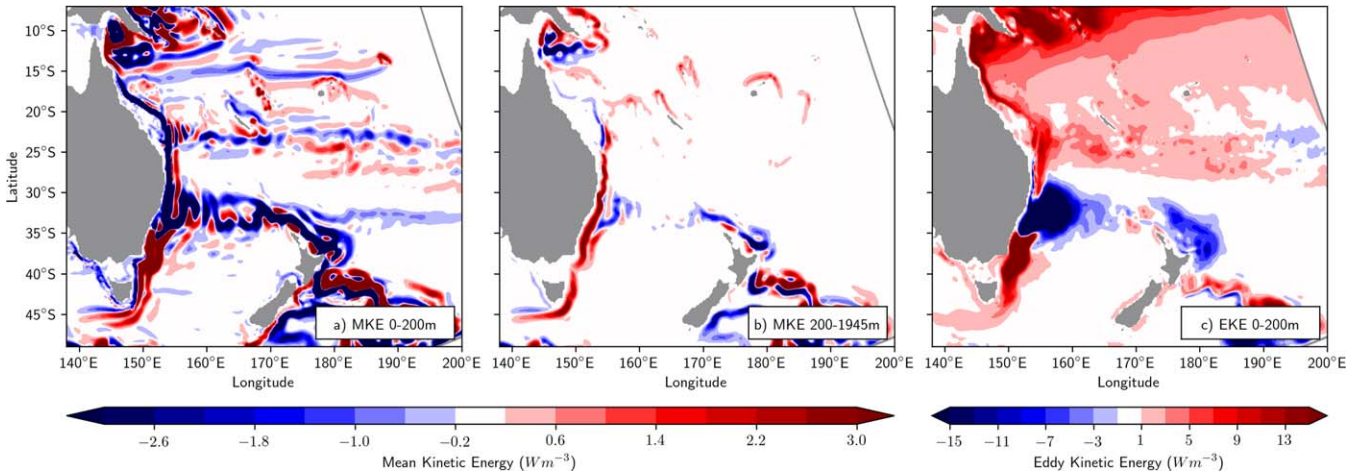

Figure 8. Change in VARY-LOCAL (a) 0–200 m average MKE, (b) 200–1,945 m average MKE, and (c) 0–200 m average EKE relative to CONSTANT.

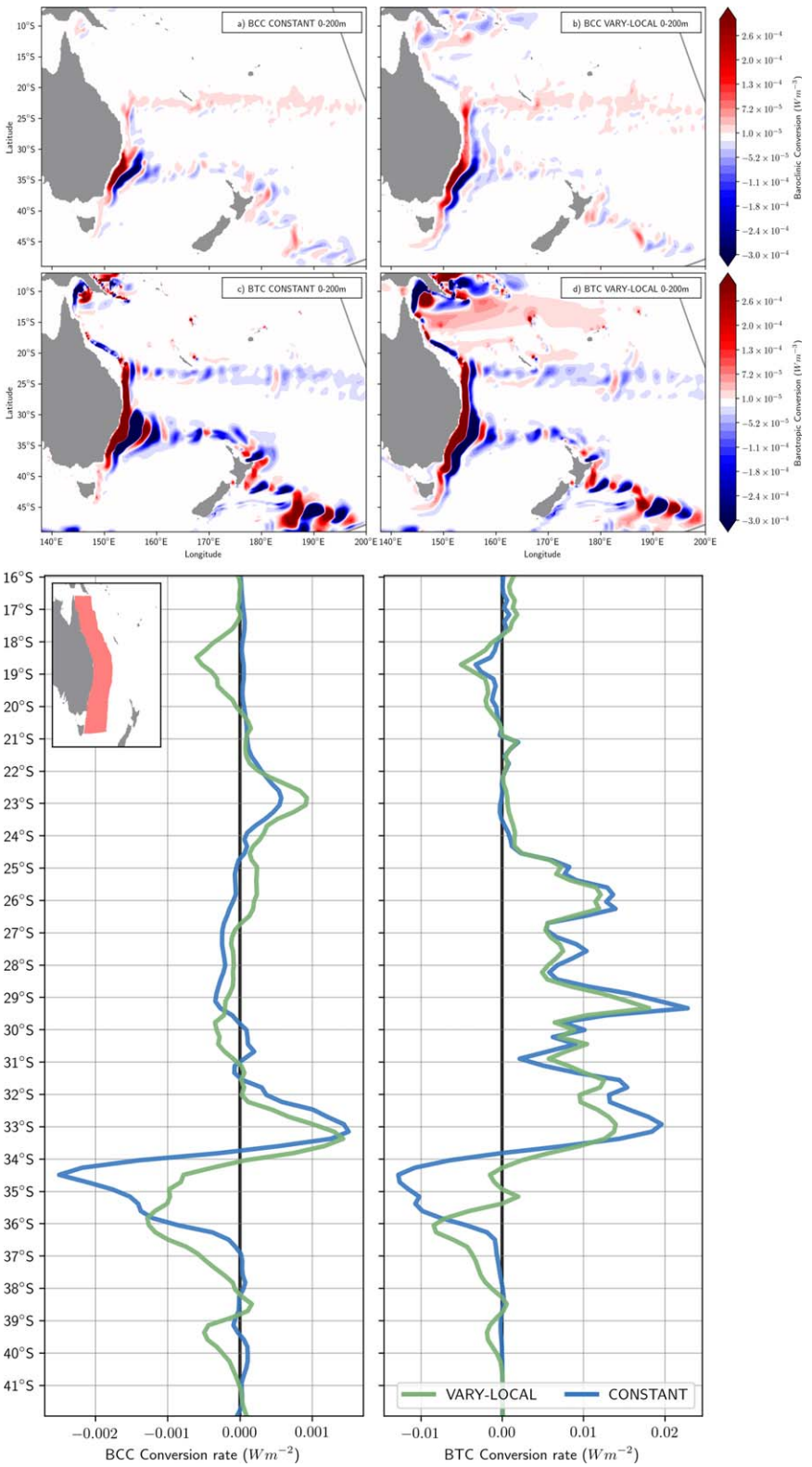

Figure 9. Baroclinic (BCC) and barotropic (BTC) conversion terms depth-averaged 0–200 m for (a, c) CONSTANT and (b, d) VARY-LOCAL. (e) BCC and (f) BTC integrated vertically over the upper 200 m and zonally over a band of 10° bounded on the west by the coastline (shaded on inset map in Figure 9e). Positive values of these terms imply mean-to-eddy energy conversion.

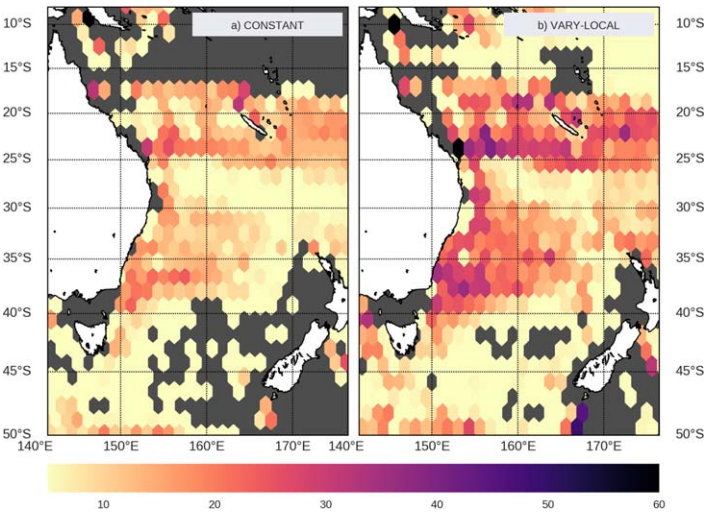

Figure 10. Total eddy count for tracked eddies with lifetimes of at least 4 days. Gray indicates areas of no data or where fewer than five eddies were detected. Eddies are only counted in each pixel or "hexbin" once in their tracked lifetime. (a) CONSTANT and (b) VARY-LOCAL experiment.

Figure 9 shows the depth averaged (surface-200 m) baroclinic (BCC) and barotropic (BTC) conversion terms (section 2.6). In both CONSTANT and VARY-LOCAL cases, consistent with previous studies (Bowen et al., 2005; Mata et al., 2006; Oliver et al., 2015), the coastal EAC region exhibits mixed barotropic/baroclinic conversion (positive values) suggesting both energy pathways are responsible for eddy generation. We now consider changes in the conversion terms first offshore, second upstream and lastly along the EAC coastal region.

Figure 9d shows a large increase in MKE → EKE (BTC) offshore of north-eastern Australia (12°S–20°S, 145°E–180°E) under local surface forcing (VARY-LOCAL). This is likely related to the established dominance of barotropic energy conversion in the region. Specifically, Qiu and Chen (2004) found that the seasonal variability of the EKE signal in the South Equatorial Current system was related to the varying strength of barotropic energy conversion and the seasonal intensity of the SECC jet. With local surface forcing variability (VARY-LOCAL) there is an increase in both MPE → EPE and EPE → MPE along the Queensland coast (Figures 9a and 9b). Finally, there are small increases in EKE → MKE (Figure 9d) and MPE → EPE (Figure 9b) south of New Caledonia. This increase in baroclinic energy conversion is located in the same position as the baroclinic waveguide south of New Caledonia discussed by O'Kane et al. (2014) and Sloyan and O'Kane (2015). The nonlinear, baroclinic flows south of New Caledonia are maintained by some of the strongest observed gradients between tropical and subtropical waters in the region (Couvelard et al., 2008).

In the upstream EAC, there is a stronger, more continuous path of both MPE → EPE and EPE → MPE energy conversion in the VARY-LOCAL simulation (Figures 9a and 9b); the inshore positive contribution suggesting increased MPE → EPE conversion is consistent with stronger upstream eddy energy shown in Figure 8c.

To look at changes along the EAC, we follow a similar integration method to Oliver et al. (2015): the coastally bound 10° offshore of the Australian continent is integrated in the upper 200 m for the BCC and BTC conversion terms, shown in Figures 9e and 9f. While this integration provides a convenient summary we note that it involves cancellation between positive and negative terms and so only highlights the net energy transfer. The biggest change is seen at ∼34.5°S, where the VARY-LOCAL experiment shows weaker conversion into the mean field (smaller negative values for both BCC and BTC), consistent with weaker EKE in the separation region in VARY-LOCAL (see Figure 8). Consistent with a stronger EAC extension, south of 36°S, VARY-LOCAL has enhanced eddy to mean flow conversion in both BCC and BTC.

Figure 10 shows large-scale differences between the eddy tracks of CONSTANT and VARY-ALL; the eddies are tracked using the method described in section 2.5. Specifically, Figure 10 shows eddies that have been tracked for at least 4 days. Compared to VARY-ALL, the CONSTANT experiment has large regions where no or fewer than five eddies were detected (gray hexbins); for example over the northern area of the domain (8°S–20°S, 140°E–175°E) and in the Tasman Sea on the western side of New Zealand. The most striking difference between the two experiments is the increase in the number of eddies upstream in the EAC and offshore into the Pacific north and south of New Caledonia (20°S–25°S, 153°E–175°E).

Figures 11a–11e present additional experiments (section 2.2) with filtered wind stress variability and all other surface and boundary fluxes held constant; Figure 11f shows the power spectrum of the spatially integrated wind stress curl with the filter band edges marked. Figure 11a closely resembles VARY-LOCAL (Figure 5a), showing that monthly to synoptic wind variability (faster than 56 days) is critically important for the rectified enhancement of the EAC extension (and also that variability of other surface fluxes is unimportant). In contrast, the lower frequency experiments in Figures 11b–11e show little change in the EAC extension extent. This is an important result because high-frequency variability is not typically associated with the extent of the EAC extension (e.g., Cai, 2006; Hill et al., 2011; Oliver & Holbrook, 2014). The importance of this high-frequency band is likely due to it containing more integrated variance than the others, despite having lower amplitude than the annual peak (see Figure 11f table; the total in the <56 days band is

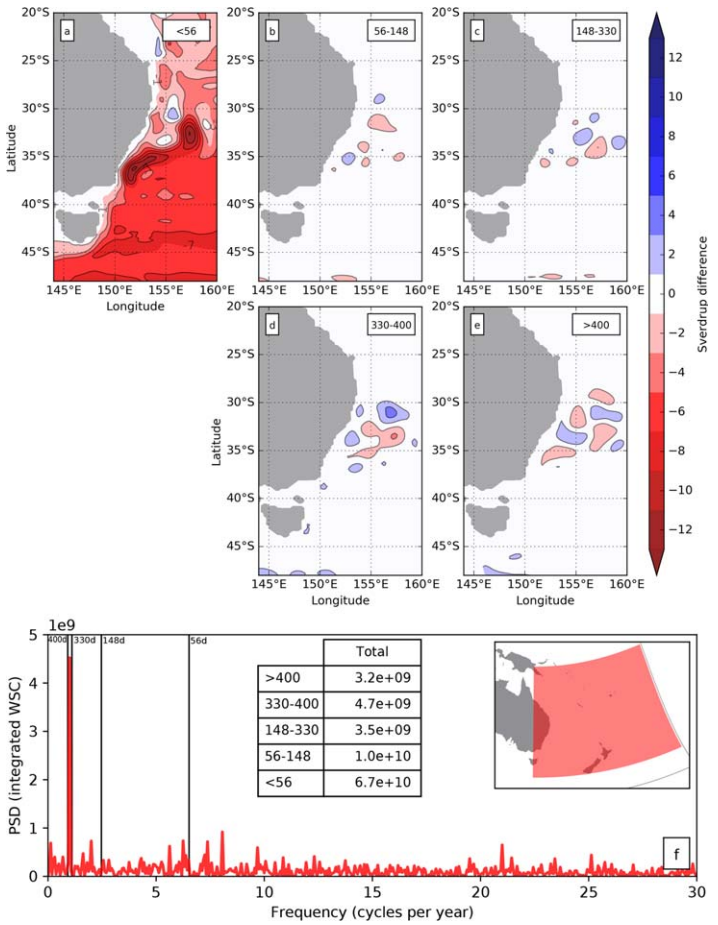

Figure 11. (a–e) Time-mean barotropic stream function difference between filtered regional wind stress experiment and CONSTANT (integration taken eastward from Australia down to 1,945 m; contours every 2 Sv; matches Figure 5a for comparison). Wind stress is filtered, retaining only periods: (a) <56 days, (b) 56–148 days, (c) 148–330 days, (d) 330–400 days, and (e) >400 days. (f) Power spectral density of the integrated wind stress curl (between January 1994 and December 2009) for south-western Pacific Ocean (shaded red in inset). Black lines indicate where the wind stress filtering occurs between experiments and the table indicates the total integrated wind stress curl for the filtered experiments 5–9 (see supporting information Table S1).

actually an underestimate, as the model output data was daily whereas the forcing was 3-hourly; in addition the spatial averaging reduces the high-frequency signal from synoptic weather).

5. Summary and Discussion

A hierarchy of ocean model simulations with the same time-mean wind stress forcing was examined to understand the impact of local and remote forcing variability on the EAC (here "local" means surface forcing over the regional domain, and "remote" means the ocean boundary forcing, see section 2.2). The modeled East Australian Current has high intrinsic variability when forced only by a time-mean steady wind field and surface fluxes. Oceanic variability through the remote ocean boundary conditions was found to have limited impact on the mean transport in the EAC extension and mean state of the Tasman Sea circulation. Given the high intrinsic variability (as shown in the CONSTANT experiment) it is unsurprising that previous studies have only found weak correlations between EAC variability and climate modes such as ENSO (Hu et al., 2015). In comparison to steady forcing, we find that variability in the local forcing field creates: a rectified subsurface enhancement of the EAC with increased eddy variance in the upstream EAC, a shorter eddy shedding time scale, and a time-mean EAC extension that extends further south toward Tasmania. Although we find no evidence of phase-locking (e.g., Kiss & Frankcombe, 2016) between the seasonal cycle of the forcing field and EAC eddy shedding, we do see a reduction in the variability of the eddy-shedding timing under variable surface forcing (supporting information Figure S3). Additional experiments (Figure 11) reveal that regional variability in the wind stress field shorter than 56 days accounts for the enhancement of the mean EAC extension, and that variability at longer time scales and/or in other surface fluxes is unimportant for this feature.

The impact of time-varying forcing (with the same time-mean) on the extent of the EAC extension has implications for climate change simulations in the Tasman Sea. Coastal downstream EAC extension sections JK and AB show a mean transport change of 7.4 and 5.5 Sv, respectively, between steady forcing (CONSTANT) and variable forcing (VARY-ALL) experiments. With a maximum standard error in the mean of 1.5 Sv, these changes are statistically significant. This is an important result as these are similar to the long-term changes in transports predicted by recent climate change simulations both in an eddy-resolving model (4.3 Sv at section AB (Oliver & Holbrook, 2014) and the multi-model mean from 33 CMIP5 coupled simulations (6.8 Sv between 35°S and 45°S (Sen Gupta et al., 2016)). Both these studies look at changes in a time-mean component of the wind stress curl (not the varying part) to explain simulated changes to the EAC extension, an assumption that is not uncommon (e.g., Cai, 2006; Feng et al., 2016; Hill et al., 2011). The present study suggests that long term trends in local, *high-frequency* variability (<56 days) are an important additional nonlinear consideration for climate change studies focusing on the spinup of the EAC.

The EAC inflows and formation regions are highly nonlinear and baroclinic (Couvelard et al., 2008; Qiu & Chen, 2004; Srinivasan et al., 2017; Webb, 2000). There is mounting evidence that WBCs are not strengthening in a time-mean Sverdrup-like response but rather with enhanced eddy fields (Beal & Elipot, 2016; Ganachaud et al., 2014; Sloyan & O'Kane, 2015). We offer additional dynamical insight into the historical spin-up/decadal variability mechanism put forward by O'Kane et al. (2014) and Sloyan and O'Kane (2015) and endorsed by Oliver et al. (2015) in an eddy-resolving future climate simulation. Specifically, we find evidence

that appears consistent with parts of the mechanism presented in Sloyan and O'Kane (2015), namely that nonlinear baroclinic offshore variability drives modest changes in the upstream EAC but strong changes in the EAC-extension, Tasman Sea stratification and thermocline depth (supporting information Figure S4). Our study extends Sloyan and O'Kane (2015) by using an eddy-permitting model. We also find a subsurface increase in MKE along the whole length of the EAC forced by local wind variability of time scales $<$56 days, rather than the low-frequency remote forcing implied by Sloyan and O'Kane (2015). Unlike Sloyan and O'Kane (2015), we do not find that a weaker EAC transport at 28°S leads to a weaker EAC extension; however, we do find the well documented anticorrelation of the Tasman Front and EAC extension transports (e.g., Hill et al., 2011). Future work could examine the role of resolution and realistic wind perturbations in the EAC extension and Tasman Front pathways (e.g., Holton et al., 2016; Loveday et al., 2014; Seager & Simpson, 2016).

Qiu and Chen (2004) suggested that the annual cycle of the South Equatorial Countercurrent's EKE was similar in phase and amplitude to the EAC, starting a discussion in the literature on whether the EAC was influenced by offshore variability. While there is evidence of EAC variability being determined by offshore variability on decadal time scales (Hill et al., 2008; Holbrook et al., 2011), there has been little evidence of forced variability at mesoscale or eddy-shedding time scales (Bowen et al., 2005; Mata et al., 2006). Consistent with Bowen et al. (2005) and Mata et al. (2006), our study finds that the EAC sheds eddies due to intrinsically generated mixed barotropic/baroclinic instabilities; we extend this paradigm by showing that the spatial location and conversion rate of instability can be influenced by local surface forcing variability. While beyond the scope of this paper, an interesting extension would refine the size of the local surface forcing (i.e., spatially modify the forcing area from VARY-LOCAL) and qualify the importance of remote higher-period variability ($>$5 day means). In addition, the change in eddy shedding behavior would benefit from a more detailed energetics analysis (e.g., Kang & Curchitser, 2015; Jouanno et al., 2016; Munday & Zhai, 2017; Zhao et al., 2016; Zhong et al., 2016).

Mesoscale ocean-atmosphere interactions are increasingly recognized as important for the pathway and extension of WBCs (e.g., Ma et al., 2016; Renault et al., 2016a, 2017). Here we have studied the simplest scenario, uncoupled simulations under prescribed variable surface flux forcing (no bulk formulae); the simulations shown in Figure 11 also have no variability in buoyancy fluxes. By design then, this excludes: nonlinear feedback of air-sea turbulent fluxes (see Hogg et al., 2009; Wu et al., 2016) and in particular the "eddy-killing effect," nonlinearity in the stress formula, and relative wind (e.g., Dawe & Thompson, 2006; Renault et al., 2016b; Zhai, 2013; Zhai et al., 2012). Future work could look at the sensitivity of the EAC extension extent to high-frequency forcing in more realistic frameworks. Given the increasing evidence for a South Pacific gyre in a transitional state responding to an evolving wind forcing (Roemmich et al., 2016; Yang et al., 2016), this kind of research is crucial if we wish to understand the past and future circulation of the Tasman Sea.

Acknowledgments
This work was supported by an Australian Government Research Training Program Scholarship and the Australian Research Council (ARC), specifically, the ARC Centre of Excellence in Climate System Science (CE110001028) and grant DE130101336. This research was undertaken with the assistance of resources from the National Computational Infrastructure (NCI), which is supported by the Australian Government. We thank Eric C. J. Oliver for developing the eddy tracking code (Oliver et al., 2013, Appendix A); the GitHub fork used in this study is publicly available online (https://github.com/chrisb13/eddyTracking). NJ is funded by the French National Research Agency through the TROIS-AS project (ANR-15-CE01-0005-01).

References

Amante, C., & Eakins, B. W. (2009). *ETOPO1 1 arc-minute global relief model: Procedures, data sources and analysis* (NOAA Tech. Memo. NESDIS NGDC-24). Silver Spring, MD: NOAA. https://doi.org/10.1594/PANGAEA.769615

Andres, M., Yang, J., & Kwon, Y.-O. (2012). Adjustment of a wind-driven two-layer system with mid-basin topography. *Journal of Marine Research*, *70*(6), 851–882. https://doi.org/10.1357/002224012806770946

Barnier, B., Dussin, R., & Molines, J. M. (2011). *Scientific validation report (ScVR) for V1 reprocessed analysis and reanalysis. WP 04 – GLO – CNRS_LEGI Grenoble*. MyOcean.

Barnier, B., LeSommer, J., Molines, J.-M., Penduff, T., Theetten, S., Treguier, A.-M., . . . Myers, P. (2007). Eddy-permitting ocean circulation hindcasts of past decades. *CLIVAR-Exchanges*, *12*, 8–10.

Barnier, B., Madec, G., Penduff, T., Molines, J.-M., Treguier, A.-M., Le Sommer, J., . . . De Cuevas, B. (2006). Impact of partial steps and momentum advection schemes in a global ocean circulation model at eddy-permitting resolution. *Ocean Dynamics*, *56*(5–6), 543–567. https://doi.org/10.1007/s10236-006-0082-1

Barnier, B., Marchesiello, P., De Miranda, A. P., & Molines, J. (1998). A sigma-coordinate primitive equation model for studying the circulation in the South Atlantic. Part I: Model configuration with error estimates. *Deep Sea Research Part I: Oceanographic Research Papers*, *45*, 543–572.

Beal, L. M., & Elipot, S. (2016). Broadening not strengthening of the Agulhas Current since the early 1990s. *Nature*, *540*, 570–573. https://doi.org/10.1038/nature19853

Bernie, D. J., Woolnough, S. J., Slingo, J. M., & Guilyardi, E. (2005). Modeling diurnal and intraseasonal variability of the ocean mixed layer. *Journal of Climate*, *18*(8), 1190–1202. https://doi.org/10.1175/JCLI3319.1

Böning, C. W., & Budich, R. G. (1992). Eddy dynamics in a primitive equation model: Sensitivity to horizontal resolution and friction. *Journal of Physical Oceanography*, *22*, 361–381.

Bowen, M. M., Wilkin, J. L., & Emery, W. J. (2005). Variability and forcing of the East Australian Current. *Journal of Geophysical Research*, *110*, C03019. https://doi.org/10.1029/2004JC002533

Cai, W. (2006). Antarctic ozone depletion causes an intensification of the Southern Ocean super-gyre circulation. *Geophysical Research Letters*, *33*, L03712. https://doi.org/10.1029/2005GL024911

Cai, W., Shi, G., Cowan, T., Bi, D., & Ribbe, J. (2005). The response of the Southern Annular Mode, the East Australian Current, and the southern mid-latitude ocean circulation to global warming. *Geophysical Research Letters*, *32*, L23706. https://doi.org/10.1029/2005GL024701

Cetina-Heredia, P., Roughan, M., van Sebille, E., & Coleman, M. A. (2014). Long-term trends in the East Australian Current separation latitude and eddy driven transport. *Journal of Geophysical Research: Oceans*, *119*, 4351–4366. https://doi.org/10.1002/2014JC010071

Chelton, D. B., Schlax, M. G., & Samelson, R. M. (2011). Global observations of nonlinear mesoscale eddies. *Progress in Oceanography*, *91*(2), 167–216. https://doi.org/10.1016/j.pocean.2011.01.002

Chiswell, S. M., & Sutton, P. J. (2015). Drifter- and float-derived mean circulation at the surface and 1000 m in the New Zealand region. *New Zealand Journal of Marine and Freshwater Research*, *49*(2), 259–277. https://doi.org/10.1080/00288330.2015.1008522

Couvelard, X., Marchesiello, P., Gourdeau, L., & Lefèvre, J. (2008). Barotropic zonal jets induced by islands in the Southwest Pacific. *Journal of Physical Oceanography*, *38*(10), 2185–2204. https://doi.org/10.1175/2008JPO3903.1

Dawe, J. T., & Thompson, L. A. (2006). Effect of ocean surface currents on wind stress, heat flux, and wind power input to the ocean. *Geophysical Research Letters*, *33*, L09604. https://doi.org/10.1029/2006GL025784

Dee, D. P., Uppala, S. M., Simmons, A. J., Berrisford, P., Poli, P., Kobayashi, S., . . . Vitart, F. (2011). The ERA-Interim reanalysis: Configuration and performance of the data assimilation system. *Quarterly Journal of the Royal Meteorological Society*, *137*(656), 553–597. https://doi.org/10.1002/qj.828

Doddridge, E. W., Marshall, D. P., & Hogg, A. M. (2016). Eddy cancellation of the Ekman cell in subtropical gyres. *Journal of Physical Oceanography*, *46*(10), 2995–3010. https://doi.org/10.1175/JPO-D-16-0097.1

Eden, C., & Böning, C. (2002). Sources of eddy kinetic energy in the Labrador Sea. *Journal of Physical Oceanography*, *32*(12), 3346–3363. https://doi.org/10.1175/1520-0485(2002)032<3346:SOEKEI>2.0.CO;2

Everett, J. D., Baird, M. E., Oke, P. R., & Suthers, I. M. (2012). An avenue of eddies: Quantifying the biophysical properties of mesoscale eddies in the Tasman Sea. *Geophysical Research Letters*, *39*, L16608. https://doi.org/10.1029/2012GL053091

Feng, M., Zhang, X., Oke, P., Monselesan, D., Chamberlain, M., Matear, R., & Schiller, A. (2016). Invigorating ocean boundary current systems around Australia during 1979–2014: As simulated in a near-global eddy-resolving ocean model. *Journal of Geophysical Research: Oceans*, *121*, 3395–3408. https://doi.org/10.1002/2016JC011842

Fransner, S. F. (2012). *Effect of model settings on western boundary currents in an eddy resolving model*. Saint-Martin-d'Hères, France: Université Joseph Fourier -Grenoble 1.

Ganachaud, A., Cravatte, S., Melet, A., Schiller, A., Holbrook, N. J., Sloyan, B. M., . . . Send, U. (2014). The Southwest Pacific Ocean circulation and climate experiment (SPICE). *Journal of Geophysical Research: Oceans*, *119*, 7660–7686. https://doi.org/10.1002/2013JC009678

Godfrey, J. S. (1989). A Sverdrup model of the depth-integrated flow for the world ocean allowing for island circulations. *Geophysical & Astrophysical Fluid Dynamics*, *45*(1–2), 89–112. https://doi.org/10.1080/03091928908208894

Gray, A. R., & Riser, S. C. (2014). A global analysis of Sverdrup balance using absolute geostrophic velocities from Argo. *Journal of Physical Oceanography*, *44*(4), 1213–1229. https://doi.org/10.1175/JPO-D-12-0206.1

Haidvogel, D. B., & Beckmann, A. (1999). *Numerical ocean circulation modeling*. London, UK: Imperial College Press.

Hill, K. L., Rintoul, S. R., Coleman, R., & Ridgway, K. R. (2008). Wind forced low frequency variability of the East Australia Current. *Geophysical Research Letters*, *35*, L08602. https://doi.org/10.1029/2007GL032912

Hill, K. L., Rintoul, S. R., Oke, P. R., & Ridgway, K. (2010). Rapid response of the East Australian Current to remote wind forcing: The role of barotropic-baroclinic interactions. *Journal of Marine Research*, *68*(3), 413–431. https://doi.org/10.1357/002224010794657218

Hill, K. L., Rintoul, S. R., Ridgway, K. R., & Oke, P. R. (2011). Decadal changes in the South Pacific western boundary current system revealed in observations and ocean state estimates. *Journal of Geophysical Research*, *116*, C01009. https://doi.org/10.1029/2009JC005926

Hogg, A. M., Dewar, W. K., Berloff, P., Kravtsov, S., & Hutchinson, D. K. (2009). The effects of mesoscale ocean-atmosphere coupling on the large-scale ocean circulation. *Journal of Climate*, *22*(15), 4066–4082. https://doi.org/10.1175/2009JCLI2629.1

Holbrook, N. J., Goodwin, I. D., McGregor, S., Molina, E., & Power, S. B. (2011). ENSO to multi-decadal time scale changes in East Australian Current transports and Fort Denison sea level: Oceanic Rossby waves as the connecting mechanism. *Deep Sea Research, Part II: Topical Studies in Oceanography*, *58*(5), 547–558. https://doi.org/10.1016/j.dsr2.2010.06.007

Holton, L., Deshayes, J., Backeberg, B. C., Loveday, B. R., Hermes, J. C., & Reason, C. J. C. (2016). Spatio-temporal characteristics of Agulhas leakage: A model inter-comparison study. *Climate Dynamics*, *48*(7), 1–15. https://doi.org/10.1007/s00382-016-3193-5

Hu, D., Wu, L., Cai, W., Gupta, A. S., Ganachaud, A., Qiu, B., . . . Kessler, W. S. (2015). Pacific western boundary currents and their roles in climate. *Nature*, *522*(7556), 299–308. https://doi.org/10.1038/nature14504

Jackett, D. R., & McDougall, T. J. (1994). Minimal adjustment of hydrographic profiles to achieve static stability. *Journal of Atmospheric and Oceanic Technology*, *12*, 381–389. https://doi.org/10.1175/1520-0426(1995)012<0381:MAOHPT>2.0.CO;2

Jouanno, J., Capet, X., Madec, G., Roullet, G., & Klein, P. (2016). Dissipation of the energy imparted by mid-latitude storms in the Southern Ocean. *Ocean Science*, *12*(3), 743–769. https://doi.org/10.5194/os-12-743-2016

Kang, D., & Curchitser, E. N. (2015). Energetics of eddy-mean flow interactions in the Gulf Stream region. *Journal of Physical Oceanography*, *45*, 1103–1120. https://doi.org/10.1175/JPO-D-14-0200.1

Kiss, A., & Frankcombe, L. M. (2016). The influence of periodic forcing on the time dependence of western boundary currents: Phase-locking, chaos, and the origins of low-frequency variability. *Journal of Physical Oceanography*, *46*(4), 1117–1136. https://doi.org/10.1175/JPO-D-15-0113.1

Kiss, A. E. (2010). Dynamics of separating western boundary currents in ocean models. *IOP Conference Series: Earth and Environmental Science*, *11*, 12034. https://doi.org/10.1088/1755-1315/11/1/012034

Large, W. G., & Yeager, S. G. (2004). *Diurnal to decadal global forcing for ocean and sea–ice models: The data sets and flux climatologies* (NCAR Tech. Note TN-460+ST, 105 pp.). Boulder, CO: National Center for Atmospheric Research. https://doi.org/10.5065/D6KK98Q6

Le Sommer, J., Penduff, T., Theetten, S., Madec, G., & Barnier, B. (2009). How momentum advection schemes influence current-topography interactions at eddy permitting resolution. *Ocean Modelling*, *29*(1), 1–14. https://doi.org/10.1016/j.ocemod.2008.11.007

Levitus, S., Conkright, M., Boyer, T., O'Brien, T., Antonov, J., Stephens, C., . . . Gelfeld, R. (1998). World Ocean Database 1998, volume 1: Introduction. In *NOAA Atlas NESDIS 18* (Vol. 1, 346 pp.). Washington, DC: U.S. Government Printing Office.

Loveday, B. R., Durgadoo, J. V., Reason, C. J. C., Biastoch, A., & Penven, P. (2014). Decoupling of the Agulhas leakage from the Agulhas Current. *Journal of Physical Oceanography*, *44*, 1776–1797. https://doi.org/10.1175/JPO-D-13-093.1

Ma, X., Jing, Z., Chang, P., Liu, X., Montuoro, R., Small, R. J., . . . Wu, L. (2016). Western boundary currents regulated by interaction between ocean eddies and the atmosphere. *Nature*, *535*(7613), 533–537. https://doi.org/10.1038/nature18640

Madec, G. (2012). *NEMO ocean engine, Note du Pôle modélisation* (Vol. 27, 357 pp.). Paris, France: Institut Pierre-Simon Laplace.

Marchesiello, P., Mcwilliams, J. C., & Shchepetkin, A. (2001). Open boundary conditions for long-term integration of regional oceanic models. *Ocean Modelling*, *3*, 1–20.

Marchesiello, P., & Middleton, J. H. (2000). Modeling the East Australian Current in the Western Tasman Sea. *Journal of Physical Oceanography*, *30*(11), 2956–2971. https://doi.org/10.1175/1520-0485(2001)031<2956:MTEACI>2.0.CO;2

Mata, M. M., Tomczak, M., Wijffels, S., & Church, J. A. (2000). East Australian Current volume transports at 30°S: Estimates from the World Ocean Circulation Experiment hydrographic sections PR11/P6 and the PCM3 current meter array. *Journal of Geophysical Research*, *105*(C12), 28509–28526. https://doi.org/10.1029/1999JC000121

Mata, M. M., Wijffels, S. E., Church, J. A., & Tomczak, M. (2006). Eddy shedding and energy conversions in the East Australian Current. *Journal of Geophysical Research*, *111*, C09034. https://doi.org/10.1029/2006JC003592

Munday, D. R., & Zhai, X. (2017). The impact of atmospheric storminess on the sensitivity of Southern Ocean Circulation to wind stress changes. *Ocean Modelling*, *115*, 14–26. https://doi.org/10.1016/j.ocemod.2017.05.005

Nilsson, C. S., & Cresswell, G. R. (1980). The formation and evolution of East Australian Current warm-core eddies. *Progress in Oceanography*, *9*(3), 133–183. https://doi.org/10.1016/0079-6611(80)90008-7

O'Kane, T. J., Matear, R. J., Chamberlain, M. A., Oliver, E. C. J., & Holbrook, N. J. (2014). Storm tracks in the Southern Hemisphere subtropical oceans. *Journal of Geophysical Research: Oceans*, *119*, 6078–6100. https://doi.org/10.1002/2014JC010192

Oliver, E. C. J., & Holbrook, N. J. (2014). Extending our understanding of South Pacific gyre "spin-up": Modeling the East Australian Current in a future climate. *Journal of Geophysical Research: Oceans*, *119*, 2788–2805. https://doi.org/10.1002/2013JC009591

Oliver, E. C. J., O'Kane, T. J., Holbrook, N. J., Kane, T. J. O., & Holbrook, N. J. (2015). Projected changes to Tasman Sea eddies in a future climate. *Journal of Geophysical Research: Oceans*, *120*, 2331–2349. https://doi.org/10.1002/2015JC010993

Oliver, E. C. J., Wotherspoon, S. J., Chamberlain, M. A., & Holbrook, N. J. (2013). Projected Tasman Sea extremes in sea surface temperature through the twenty-first century. *Journal of Climate*, *27*, 1980–1998. https://doi.org/10.1175/JCLI-D-13-00259.1

Pedlosky, J. (1965). A study of the time dependent ocean circulation. *Journal of the Atmospheric Sciences*, *22*, 267–272.

Pedlosky, J. (1996). *Ocean circulation theory*. Berlin, Germany: Springer.

Penduff, T., Juza, M., Barnier, B., Zika, J., Dewar, W. K., Treguier, A. M., . . . Audiffren, N. (2011). Sea level expression of intrinsic and forced ocean variabilities at interannual time scales. *Journal of Climate*, *24*(21), 5652–5670. https://doi.org/10.1175/JCLI-D-11-00077.1

Penduff, T., Le Sommer, J., Barnier, B., Treguier, A-M., Molines, J.-M., & Madec, G. (2007). Influence of numerical schemes on current-topography interactions in 1/4° global ocean simulations. *Ocean Science Discussions*, *4*(3), 491–528. https://doi.org/10.5194/osd-4-491-2007

Qiu, B., & Chen, S. (2004). Seasonal modulations in the eddy field of the South Pacific Ocean. *Journal of Physical Oceanography*, *34*(7), 1515–1527. https://doi.org/10.1175/1520-0485(2004)034<1515:SMITEF>2.0.CO;2

Renault, L., McWilliams, J. C., & Penven, P. (2017). Modulation of the Agulhas Current retroflection and leakage by oceanic current interaction with the atmosphere in coupled simulations. *Journal of Physical Oceanography*, *47*, 2077–2100. https://doi.org/10.1175/JPO-D-16-0168.1

Renault, L., Molemaker, M. J., Gula, J., Masson, S., & McWilliams, J. C. (2016a). Control and stabilization of the Gulf Stream by oceanic current interaction with the atmosphere. *Journal of Physical Oceanography*, *46*, 3439–3453. https://doi.org/10.1175/JPO-D-16-0115.1

Renault, L., Molemaker, M. J., McWilliams, J. C., Shchepetkin, A. F., Lemarié, F., Chelton, D., . . . Hall, A. (2016b). Modulation of wind work by oceanic current interaction with the atmosphere. *Journal of Climate*, *46*, 1685–1704. https://doi.org/10.1175/JPO-D-15-0232.1

Rhines, P. B., & Schopp, R. (1991). The wind-driven circulation: Quasi-geostrophic simulations and theory for nonsymmetric winds. *Journal of Physical Oceanography*, *21*(9), 1438–1469. https://doi.org/10.1175/1520-0485(1991)021<1438:TWDCQG>2.0.CO;2

Ridgway, K., & Dunn, J. (2003). Mesoscale structure of the mean East Australian Current system and its relationship with topography. *Progress in Oceanography*, *56*(2), 189–222. https://doi.org/10.1016/S0079-6611(03)00004-1

Ridgway, K., Dunn, J. R., & Wilkin, J. L. (2002). Ocean interpolation by four-dimensional weighted least squares—Application to the waters around Australasia. *Journal of Atmospheric and Oceanic Technology*, *19*(9), 1357–1375.

Ridgway, K. R. (2007). Long-term trend and decadal variability of the southward penetration of the East Australian Current. *Geophysical Research Letters*, *34*, L13613. https://doi.org/10.1029/2007GL030393

Ridgway, K. R., & Dunn, J. R. (2007). Observational evidence for a Southern Hemisphere oceanic supergyre. *Geophysical Research Letters*, *34*, L13612. https://doi.org/10.1029/2007GL030392

Ridgway, K. R., & Godfrey, J. S. (1994). Mass and heat budgets in the East Australian Current: A direct approach. *Journal of Geophysical Research*, *99*(C2), 3231–3248.

Ridgway, K. R., & Godfrey, J. S. (1997). Seasonal cycle of the East Australian Current. *Journal of Geophysical Research*, *102*(C10), 22921. https://doi.org/10.1029/97JC00227

Roemmich, D., Gilson, J., Davis, R., Sutton, P., Wijffels, S., & Riser, S. (2007). Decadal spinup of the South Pacific subtropical gyre. *Journal of Physical Oceanography*, *37*(2), 162–173. https://doi.org/10.1175/JPO3004.1

Roemmich, D., Gilson, J., Sutton, P., & Zilberman, N. (2016). Multidecadal change of the South Pacific gyre circulation. *Journal of Physical Oceanography*, *46*(6), 1871–1883. https://doi.org/10.1175/JPO-D-15-0237.1

Seager, R., & Simpson, I. R. (2016). Western boundary currents and climate change. *Journal of Geophysical Research: Oceans*, *121*, 7212–7214. https://doi.org/10.1002/2016JC012156

Sen Gupta, A., McGregor, S., van Sebille, E., Ganachaud, A., Brown, J., & Santoso, A. (2016). Future changes to the Indonesian Throughflow and Pacific circulation: The differing role of wind and deep circulation changes. *Geophysical Research Letters*, *43*, 1669–1678. https://doi.org/10.1002/2016GL067757

Sérazin, G., Penduff, T., Grégorio, S., Barnier, B., Molines, J.-M., & Terray, L. (2015). Intrinsic Variability of sea level from global ocean simulations: Spatiotemporal scales. *Journal of Climate*, *28*(10), 4279–4292. https://doi.org/10.1175/JCLI-D-14-00554.1

Sloyan, B. M., & O'Kane, T. J. (2015). Drivers of decadal variability in the Tasman Sea. *Journal of Geophysical Research: Oceans*, *120*, 3193–3210. https://doi.org/10.1002/2014JC010550

Sloyan, B. M., Ridgway, K. R., & Cowley, R. (2016). The East Australian Current and property transport at 27°S from 2012–2013. *Journal of Physical Oceanography*, *46*, 993–1008. https://doi.org/10.1175/JPO-D-15-0052.1

Speich, S., Blanke, B., & Cai, W. (2007). Atlantic meridional overturning circulation and the Southern Hemisphere supergyre. *Geophysical Research Letters*, *34*, L23614. https://doi.org/10.1029/2007GL031583

Srinivasan, K., McWilliams, J. C., Renault, L., Hristova, H. G., Molemaker, J., & Kessler, W. S. (2017). Topographic and mixed layer submesoscale currents in the near-surface southwestern tropical Pacific. *Journal of Physical Oceanography*, *47*(6), 1221–1242. https://doi.org/10.1175/JPO-D-16-0216.1

Stammer, D., & Wunsch, C. (1999). Temporal changes in eddy energy of the oceans. *Deep Sea Research, Part II: Topical Studies in Oceanography*, *46*(1–2), 77–108. https://doi.org/10.1016/S0967-0645(98)00106-4

Stewart, K. D., Hogg, A. M., Griffies, S. M., & Heerdegen, A. P. (2017). Vertical resolution of baroclinic modes in global ocean models. *Ocean Modelling*, *113*, 50–65. https://doi.org/10.1016/j.ocemod.2017.03.012

Stewart, K. D., Spence, P., Waterman, S., Sommer, J. L., Molines, J. M., Lilly, J. M., & England, M. H. (2015). Anisotropy of eddy variability in the global ocean. *Ocean Modelling*, *95*, 53–65. https://doi.org/10.1016/j.ocemod.2015.09.005

Sutton, P. J. H., & Bowen, M. (2014). Flows in the Tasman Front south of Norfolk Island. *Journal of Geophysical Research: Oceans*, *119*, 3041–3053. https://doi.org/10.1002/2013JC009543

Sverdrup, H. U. (1947). Wind-driven currents in a Baroclinic Ocean; with application to the equatorial currents of the Eastern Pacific. *Proceedings of the National Academy of Sciences of the United States of America*, *33*(11), 318–326.

Thomas, M. D., De Boer, A. M., Johnson, H. L., & Stevens, D. P. (2014). Spatial and temporal scales of Sverdrup balance. *Journal of Physical Oceanography*, *44*(10), 2644–2660. https://doi.org/10.1175/JPO-D-13-0192.1

Tomczak, M., & Godfrey, J. S. (2003). *Regional oceanography: An introduction*. New Delhi, India: Daya Publishing House.

van Sebille, E., England, M. H., Zika, J. D., & Sloyan, B. M. (2012). Tasman leakage in a fine-resolution ocean model. *Geophysical Research Letters*, *39*, L06601. https://doi.org/10.1029/2012GL051004

Veronis, G. (1970). Effect of fluctuating winds on ocean circulation. *Deep Sea Research and Oceanographic Abstracts*, *17*, 421–434.

Verron, J., & Le Provost, C. (1991). Response of eddy-resolved general circulation numerical models to asymmetrical wind forcing. *Dynamics of Atmospheres and Oceans*, *15*(6), 505–533. https://doi.org/10.1016/0377-0265(91)90002-W

Wang, X. H., Bhatt, V., & Sun, Y.-J. (2013). Study of seasonal variability and heat budget of the East Australian Current using two eddy-resolving ocean circulation models. *Ocean Dynamics*, *63*(5), 549–563. https://doi.org/10.1007/s10236-013-0605-5

Webb, D. J. J. (2000). Evidence for shallow zonal jets in the South Equatorial Current region of the Southwest Pacific. *Journal of Physical Oceanography*, *30*(4), 706–720. https://doi.org/10.1175/1520-0485(2000)030<0706:EFSZJI>2.0.CO;2

Wilkin, J. L., & Zhang, W. G. (2007). Modes of mesoscale sea surface height and temperature variability in the East Australian Current. *Journal of Geophysical Research*, *112*, C01013. https://doi.org/10.1029/2006JC003590

Willebrand, J., Philander, S. G. H., & Pacanowski, R. C. (1980). The oceanic response to large-scale atmospheric disturbances. *Journal of Physical Oceanography*, *10*(3), 411–429. https://doi.org/10.1175/1520-0485(1980)010<0411:TORTLS>2.0.CO;2

Wu, L., Cai, W., Zhang, L., Nakamura, H., Timmermann, A., Joyce, T., . . . Giese, B. (2012). Enhanced warming over the global subtropical western boundary currents. *Nature Climate Change*, *2*(3), 161–166. https://doi.org/10.1038/nclimate1353

Wu, Y., Zhai, X., & Wang, Z. (2016). Impact of synoptic atmospheric forcing on the mean ocean circulation. *Journal of Climate*, *29*(16), 5709–5724. https://doi.org/10.1175/JCLI-D-15-0819.1

Yang, H., Lohmann, G., Wei, W., Dima, M., Ionita, M., & Liu, J. (2016). Intensification and poleward shift of subtropical western boundary currents in a warming climate. *Journal of Geophysical Research: Oceans*, *121*, 4928–4945. https://doi.org/10.1002/2015JC011513

Ypma, S. L., van Sebille, E., Kiss, A. E., & Spence, P. (2016). The separation of the East Australian Current: A Lagrangian approach to potential vorticity and upstream control. *Journal of Geophysical Research: Oceans*, *121*, 758–774. https://doi.org/10.1002/2014JC010632

Zhai, X. (2013). On the wind mechanical forcing of the ocean general circulation. *Journal of Geophysical Research: Oceans*, *118*, 6561–6577. https://doi.org/10.1002/2013JC009086

Zhai, X., Johnson, H. L., Marshall, D. P., & Wunsch, C. (2012). On the wind power input to the ocean general circulation. *Journal of Physical Oceanography*, *42*(8), 1357–1365. https://doi.org/10.1175/JPO-D-12-09.1

Zhao, Y.-B., Liang, X. S., & Gan, J. (2016). Nonlinear multiscale interactions and internal dynamics underlying a typical eddy-shedding event at Luzon Strait. *Journal of Geophysical Research: Oceans*, *121*, 8208–8229. https://doi.org/10.1002/2016JC012483

Zhong, L., Hua, L., & Luo, D. (2016). The eddy–mean flow interaction and the intrusion of western boundary current into the South China Sea–type basin in an idealized model. *Journal of Physical Oceanography*, *46*(8), 2493–2527. https://doi.org/10.1175/JPO-D-15-0220.1